Scaling properties and robustness of finite-size Lyapunov exponents in surface marine flows

by

Ismael Hernández Carrasco

B.S. (Universidad Autónoma de Madrid) 2006

THESIS

Presented to

The University of Balearic Islands

in Partial Fulfillment

of the Requirements

for the Degree of

MASTER OF SCIENCE

September 2009

A .....

“La electricidad será algo por lo que pedirán impuestos”

– Faraday–

Contents

Chapter 1

Motivation

Horizontal transport and mixing processes [1–3] are central to the study of the physical, chemical, and biological dynamics of the ocean. Correct understanding and precise modelling of them are relevant from a theoretical viewpoint and crucial for a range of practical issues, such as plankton dynamics or the fate of pollutant spills. In this regard, the last few years have seen the appearance of interesting new developments [4] on the Lagrangian description of transport and mixing phenomena, many of them coming from the area of nonlinear dynamics. Such approaches do not aim at predicting individual tracer trajectories, but at locating spatial structures that are known from dynamical systems theory to act as templates for the whole flow [5, 6]. This is mainly due to the capacity of the Lagrangian diagnostics to exploit the spatiotemporal variability of the velocity field by following fluid particle trajectories, at difference of Eulerian ones which analyze frozen snapshots of data. Among these Lagrangian techniques, a powerful class consists in the computation of local Lyapunov exponents (LLE) which measure the relative dispersion of transported particles [7–14]. In particular, there are the so called finite-size Lyapunov exponents (FSLEs) where one computes the time taken by two trajectories, initially separated by a finite distance, to reach a larger final finite distance [11–14].

LLEs are attracting the attention of the oceanographic community [15–20]. The main reasons for this interest are the following: a) they identify and display the dynamical structures in the flow that strongly organizes fluid motion (Lagrangian Coherent Structures (LCSs)) like vortices, barriers to transport, fronts, etc ; b) they are relatively easy to compute; c) they provide extra information on characteristics time-scales for the dynamics; d) they are able to reveal oceanic structures below the nominal resolution of the velocity field being analyzed; and e) The FSLE, in addition, is specially suited to analyze transport in closed areas [15].

Despite the growing number of applications of FSLEs, the focus of the present work, a systematic analysis of many of their properties is still lacking. In particular, the following questions remain open: how do errors in the velocity field propagate onto the FSLE? is the sub-grid information that they provide valid or just an artifact? How do they

transform under changes in scale? The main objective of this work is to address these questions. In particular with reference to their potential applications into ocean dynamics, and to the characterization of fluid transport at the mesoscale (10-100 kilometers) and at submesoscale (1-10 kilometers). To do this, we will study the FSLEs at different spatial resolutions and analyze their scaling properties and their response to different sources of error both in the velocity data and in the way that particle trajectories are computed. In order to keep close to the oceanographic applications we use numerical data of the marine surface velocity of the Mediterranean Sea, though the particular physical phenomena in the area are not our focus in this work.

This work is organized as follows. We start in Chapter 1 with an introduction in which basic tools and concepts are briefly displayed. In Chapter 2 we comment on the data and methodology that will be used along the study, and we show properties obtained from FSLE applied to the Balearic Sea. In Chapter 3 the scale invariance properties of the FSLEs are analyzed. Chapter 4 is devoted to study the influence of errors in the FSLEs fields: both errors in the velocities and errors arising from neglecting small-scale turbulence in the trajectories of the particles. Finally, in the Summary section we write down our conclusions.

Chapter 2

Concepts and Tools

In this chapter we introduce the concepts and tools, borrowed from the theory of nonlinear dynamical systems, which will help us to understand the global geometry of fluid flows, and will allow a quantitative analysis of transport and mixing in oceanic process.

2.1 Eulerian and Lagrangian descriptions

The description of fluid motion can be addressed following two different ways. One can deal at any time with velocity, pressure and density fields at any spatial point in the fluid, or either, one deals with the trajectory of each fluid particle. The first approach is usually called *Eulerian* and the second one *Lagrangian*. In principle both are equivalent, and if we denote by **v**(**x**,t) the Eulerian velocity field, which tells us the value of the fluid velocity at any space-time point (**x**,t), then the motion of a fluid particle with initial localization **x**(0) is given by

$$\frac{d\mathbf{x}}{dt} = \mathbf{v}(\mathbf{x}, t). \tag{2.1}$$

This expression establishes the physical connection between the Eulerian and Lagrangian description. It clearly reads that when a particular fluid particle is known to be at a specific space-time point, its Lagrangian velocity must be equal to the Eulerian field value at that space-time point.

2.2 Dynamical Systems

A dynamical system of general form is often expressed by

$$\frac{d\mathbf{x}}{dt} = \mathbf{v}(\mathbf{x}(t), t) \tag{2.2}$$

$$\mathbf{x}(t_0) = \mathbf{x}_0 \tag{2.3}$$

$$\frac{d\mathbf{x}}{dt} = \mathbf{v}(\mathbf{x}(t)) \tag{2.4}$$

$$\mathbf{x}(t_0) = \mathbf{x}_0 \tag{2.5}$$

In the differential Eqs. (2.2), (2.3), t represents time and it is the independent variable, and the dependent variable, $\mathbf{x}(t)$, represents the state of the system at time t. The vector function $\mathbf{v}(\mathbf{x}, t)$ typically satisfies some level of continuity. As a side note, through this introduction we will try to denote vector valued quantities by boldfaced letters.
As time evolves, solution of Eqs. (2.2), (2.3) trace out curves, or in dynamical systems terminology, they flow along their trajectory. Numerical solutions of Eqs. (2.2), (2.3) can almost always be found by numerically integrating **v**, however such solutions by themselves are not very desirable for general analysis. While the exact solution of Eqs. (2.2), (2.3) would be ideal, unless $\mathbf{v}(\mathbf{x}, t)$ is a linear function of the state **x** and independent of time t, and a few other cases, there is no general way to determine the analytic solution of Eqs. (2.2), (2.3).

If **v** is independent of time t the system is known as time-independent, or autonomous, and there are a number of standard techniques for analyzing such systems. For instance, the global flow geometry of autonomous systems can often be understood by studying invariant manifolds of the fixed points of Eqs. (2.2), (2.3), in particular stable and unstable manifolds often play a central role. These concepts are described in the following. A fixed point of **v** is a point $\mathbf{x}^c$ such that $\mathbf{v}(\mathbf{x^c}) = \mathbf{0}$. The stable manifolds of a fixed point $\mathbf{x}^c$ are all trajectories which asymptote to $\mathbf{x}^c$ when $t \to \infty$. Similarly, the unstable manifolds of $\mathbf{x}^c$ are all trajectories which asymptote to $\mathbf{x}^c$ when $t \to -\infty$. Often, stable and unstable manifolds act as separatrices, which separate distinct regions of motion, making them effective in understanding the flow geometry.

For example consider the planar, frictionless pendulum. This setup has a point mass, m, at the end of a weightless rod of length l, as shown in Fig. 2.1. The dynamics is given by the second order equation

$$\frac{d^2\theta}{dt^2} = -mgl\sin\theta(t), \tag{2.6}$$

where **g** denote the acceleration due to gravity. Since any nth-order system is equivalent to a set of first order equations, let us define $x = \theta$ and $y = \dot{\theta}$, which allows us to write Eq.(2.6) as

$$\dot{y} = -mgl\sin x\ , \dot{x} = y, \tag{2.7}$$

which places it in the first-order vector form given by Eq.(2.2).

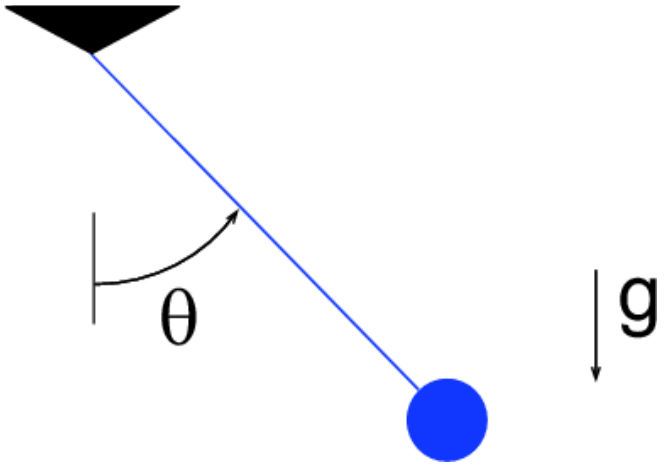

Figure 2.1: Pendulum setup

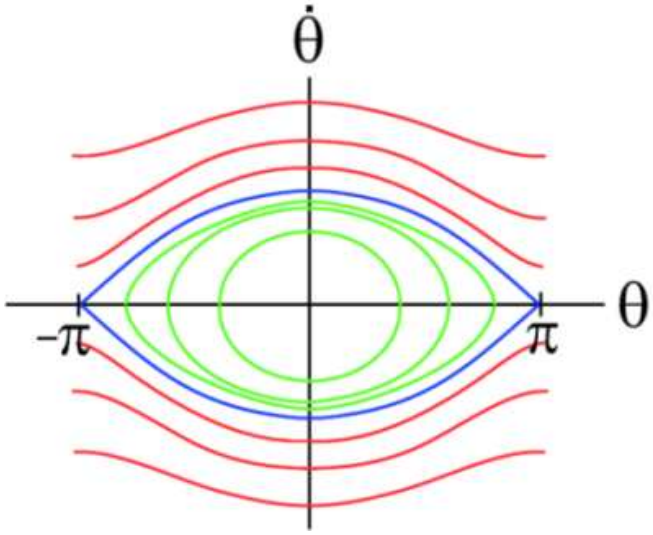

Figure 2.2: Pendulum phase portrait

The phase portrait of the pendulum is shown in Fig. 2.2. Since all values for the positions θ are repeated to a value over the interval from -π to π, we only show the phase portrait for θ ranging over this interval. If we equate positions in this manner, then technically $\theta = \pi$ is equivalent to $\theta = -\pi$, however they appear as two separate points in the phase portrait, but one can reconcile this by mentally wrapping the phase portrait around a cylinder such that $\theta = \pi$ and $\theta = -\pi$ meet up. The pendulum has fixed points at $(\theta, \dot{\theta})$=$(0, 0)$ and $(\theta, \dot{\theta})$=$(\pi, 0)$. The fixed point $(\pi, 0)$ is hyperbolic. In a system of differential equations a hyperbolic point is a stationary point such that the eigenvalues of

the linearized system have non-zero real part, and is the point where the stable and unstable manifolds intersect. We will see later that hyperbolicity plays an important role in transport. The stable and unstable manifolds of the fixed point $(\pi, 0)$ are shown in blue in Fig. 2.2 and form separatrices. These separatrices divide the flow into regions of distinct dynamics. Inside these separatrices, the pendulum oscillates back and forth. Outside the separatrices, the pendulum continually spins in one direction.

The pendulum example helps demonstrate how the stable and unstable manifolds can help uncover the global flow geometry of a dynamical system. This is one of the main reasons most introductory texts on dynamical systems dedicate time to explaining such notions and proving their existence. In fact, numerous people have researched different methods for computing, or growing, such manifolds. Many methods rely on growing manifolds from their hyperbolic fixed points. This is possible because for autonomous systems the stable and unstable manifolds of a fixed point are locally tangent to the eigenvectors of the linearized vector field about that point.

The notion of stable and unstable manifolds becomes ambiguous for time-dependent systems, which are the most relevant for us. For example, such systems rarely even have fixed points in the traditional sense, and in addition asymptotic limits for such systems are often meaningless. While there are many academic examples of time-independent dynamical systems, many dynamical systems of practical importance are time-dependent, especially in cases where the dynamical system represents the motion of a fluid.

Even time-dependent dynamical systems typically have regions of dynamically distinct behavior which can be thought of as being divided by separatrices. However, for such systems these regions change over time, and hence so do the separatrices.

To find separatrices in time-dependent systems, one might take an approach similar to above and look at fixed points of the instantaneous vector field and try to grow these manifolds by seeding near an instantaneous fixed point and advecting the points according to the time-dependent vector field. While this might seem reasonable, separatrices in time-dependent flows usually are not connected to instantaneous fixed points, although they might be located nearby.

Instead of trying to directly grow these manifolds, or separatrices, let us try to indirectly obtain them. We will do this by considering the behavior of trajectories near such structures. Our indirect method will spare us from such things as first having to locate fixed points, which can itself be a formidable task (plus these points are not typically meaningful for time-dependent systems).

To get us thinking in the right direction, consider a generic hyperbolic point and its associated stable and unstable manifolds, which is depicted in Fig. 2.3. If we integrate two points that are initially on either side of a stable manifold forward in time, then these points will eventually diverge from each other. Likewise, if we started two points on either side of an unstable manifold, then these points would quickly diverge from each other if integrated backward in time. This is why these manifolds are often called separatrices, since they separate trajectories which do qualitatively different things.

Therefore we take the viewpoint that since separatrices divide regions of qualitatively

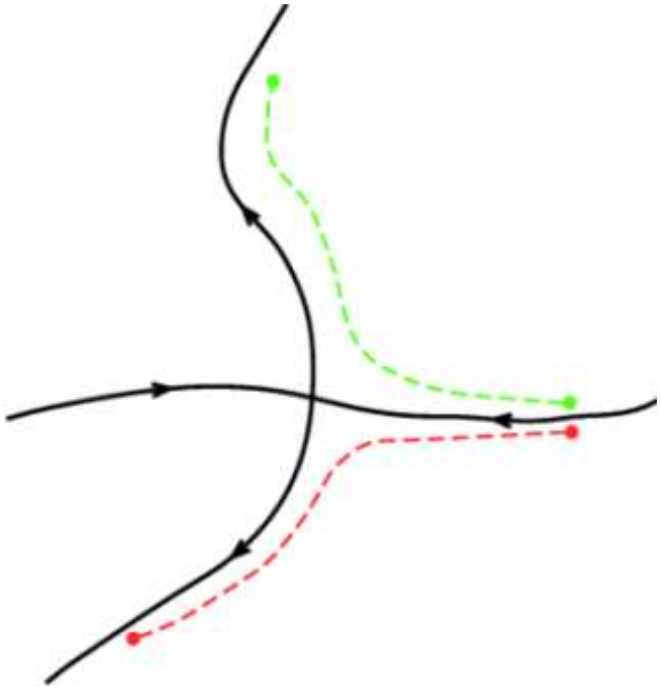

Figure 2.3: Two points on either side of a separatrix will diverge from each other

different dynamics, we can perhaps uncover or define such structures by looking at the divergence or stretching between trajectories. To find separatrices that are analogous to stable manifolds, we measure stretching forward in time and to find separatrices that are analogous to unstable manifolds, we measure stretching backward in time (Fig. 2.3). However, one should not read into the analogy between these separatrices and traditional definitions of stable and unstable manifolds too much. In fact, since the notions of stable and unstable manifolds are not well defined for time-dependent flows, we refer to theses separatrices as Lagrangian Coherent Structures (LCS), a name which is common in fluid mechanics, but its meaning is often only loosely defined. While there are numerous ways to measure ”stretching”, we have found that the Local Lyapunov Exponent (Finite-Time Lyapunov Exponent and Finite-Size Lyapunov Exponent) provides the best measure when trying to understand the flow geometry of general time-dependent systems.

2.3 The Non-asymptotic Lyapunov Exponents

The possibility of chaotic systems was first introduced by the French mathematician Henri Poincare in the 1890s in a paper on the stability of the Solar System. Some time later, other scientists found additional chaotic systems and they developed new mathematics and theories (Kovalevska, Hopf, Kolmogorov among others). In 1963, Edward Lorentz described the behavior related to chaotic attractors occurring in dissipative systems, and recognized the unpredictability of chaotic behavior in connection with the numerical solution of an atmospheric model. Chaos is a motion irregular in time, unpredictable in the long term and sensitive to initial conditions, and complex, but ordered, in the phase space: it is associated with a fractal structure. In present day literature a system is said to be chaotic if small– i.e. infinitesimal– perturbations grow exponentially with time, and this is connected to a positive Lyapunov exponent.

$$\delta\mathbf{x}(t) \sim e^{\lambda t}\delta\mathbf{x}(t_0) \tag{2.8}$$

The classical Lyapunov exponent is defined as the exponential rate of separation, averaged over infinite time, of particle trajectories initially separated infinitesimally. Consider $\mathbf{x}(t_0)$ and $\mathbf{x}(t) = \mathbf{x}(t_0) + \delta\mathbf{x}(t)$ as two particle trajectories separated initially by a distance $\delta\mathbf{x}(t_0)$. The global Lyapunov exponent is defined by

$$\lambda = \lim_{t\to\infty} \lim_{\delta\mathbf{x}(t_0)\to 0} \frac{1}{t} \ln \frac{|\delta\mathbf{x}(t)|}{|\delta\mathbf{x}(t_0)|}, \tag{2.9}$$

This number, λ, is useful for distinguishing among the various types of systems. Negative Lyapunov exponents are characteristic of stable solutions of dissipative or non-conservative systems (the damped harmonic oscillator for instance). Such systems exhibit asymptotic stability (the orbit attracts to a stable fixed point or stable periodic orbit). If λ is positive, the orbit is unstable and chaotic. Nearby points will diverge to any arbitrary separation. All neighborhoods in the phase space will eventually be visited. These points are said to be unstable. For a continuous system, the phase space would be a tangled sea of wavy lines like a pot of spaghetti.

The Lyapunov exponent is quite useful in the study of time-independent dynamical systems. The seminal works of [21, 22] were very important in laying the theory of Lyapunov exponent for time-independent systems, although the manuscript by [23] contains a good modern and comprehensive treatment of the subject. However, many dynamical systems of practical importance, especially in the realm of fluids, are time-dependent and only known over a finite interval of time and space. Because of its asymptotic nature, the classical Lyapunov exponent is not suited for analyzing time-dependent dynamical systems or those that are only defined on a finite time-space interval, so its value is quite limited for practical analysis. The infinite-time limit in Eq.(2.9) makes the Lyapunov exponent of limited practical use when dealing with experimental data. The second limit,

$\delta\mathbf{x}(t_0) \rightarrow 0$, makes it an even more difficult quantity to evaluate either experimentally or numerically. Whereas the (global) Lyapunov exponent gives a measure for the total predictability of a system, it is sometimes interesting to estimate the local predictability around a point **x** in phase space. In this case, a generalization of the Lyapunov exponent, called the Local Lyapunov exponent (LLE), has been proposed to study the growth of noninfinitesimal perturbations (distance between trajectories) in dynamical systems. Recently the concept of a LLE has been applied to study dispersion in turbulent flow fields.

The LLE is a scalar value which characterizes the amount of stretching about the trajectory of point **x** over time interval. For most flows of practical importance, the LLE varies as a function of space and time. The LLE is not an instantaneous separation rate, but rather measures the average, or integrated, separation between trajectories. This distinction is important because in time-dependent flows, the instantaneous velocity field often is not very revealing about actual trajectories, that is, instantaneous streamlines can quickly diverge from actual particle trajectories. However the LLE accounts for the integrated effect of the flow because it is derived from particle trajectories, and thus is more indicative of the actual transport behavior. We discuss this points in next sections. Depending on what asymptotic character is eliminated, there are two non-asymptotic Lyapunov exponents: finite-time and finite-size Lyapunov exponents.

2.3.1 Finite-Time Lyapunov Exponents (FTLEs)

Let us derive the expression for the FTLE considering the stretching between two neighboring particles. Consider an arbitrary point **x** in phase space at time t_0 advected by the flow a time interval T. Since the flow has a continuous dependence on initial conditions, we known that an arbitrary point near **x** at time t_0 will behave similarly as **x** when advected in the flow, at least locally in time. However, as time evolves, the distance $\delta\mathbf{x}(t_0)$ between this neighboring point and the point close to **x** will be $\mathbf{x}(t) = \mathbf{x}(t) + \delta\mathbf{x}(t)$, where we assume $\delta\mathbf{x}(t)$ is infinitesimal and arbitrarily oriented. After a time interval T we obtain an expression for the finite-time Lyapunov exponent (FTLE) at the initial point **x** at time t_0 with a finite integration time T:

$$\lambda_{t_0}^{T}(\mathbf{x}) = \frac{1}{|T|} \ln \frac{\delta\mathbf{x}(t_0 + T)}{\delta\mathbf{x}(t_0)}. \tag{2.10}$$

The FTLE is a function of the initial position **x** at time t_0, but if we vary t_0, then it is also a function of time.

2.3.2 Finite-Size Lyapunov Exponents (FSLEs)

If we want to know about the predictability time in the large with respect to a finite perturbation, it should be determined by a quantity analogous to the Lyapunov exponent. The natural starting point in looking for such a quantity is the time it takes for a perturbation to grow from an initial size δ to a tolerance Δ. This is called the (δ,Δ) predictability time and denote it by $T(\delta,\Delta)$. Generally speaking, the predictability time will fluctuate. The natural definition of the finite-size Lyapunov exponent is, therefore, an average of some function of the predictability time, such that if both δ and Δ are in the infinitesimal range, we will recover the usual Lyapunov exponent, and an obvious choice is then

$$\Lambda(\delta, \Delta) = \left\langle \frac{1}{T(\delta, \Delta)} \right\rangle \ln\left(\frac{\Delta}{\delta}\right). \tag{2.11}$$

In contrast to infinitesimal perturbations, for finite perturbations the threshold Δ is typically not to be taken much larger than the perturbation δ. What is interesting, and what makes finite-size Lyapunov exponents different from Lyapunov exponents for infinitesimal perturbation, is the dependence on δ.

In the Lagrangian analysis using velocity data of the ocean we say that the initial perturbation, δ, is the initial spatial separation of two particles, δ_0, (one of them placed at **x**) and the tolerance Δ is the final separation of these two particles, δ_f, and τ is the time required for two particles of fluid to separate from an initial distance of δ_0 to a final one of δ_f. Thus the expression for the FSLE at time t_0 is given by

$$\Lambda(\mathbf{x}, t_0, \delta_0, \delta_f) = \frac{1}{|\tau|} \ln \frac{\delta_f}{\delta_0}, \tag{2.12}$$

Now instead of fixing a finite integration time (FTLE), we fix a finite initial and final spatial separation between particles.

As the FSLE is a function of the initial distance δ_0 but also of the final distance δ_f, we can analyze oceanic structures at different sizes (LCS) using different δ_f values.

In the definition of Λ in Eq. (2.12), we used $|\tau|$ instead of τ because it is often the case that we are interested in computing Λ for $t > 0$ and $t < 0$, to produce LCS akin to stable and unstable manifolds, as was mentioned towards the end of the previous section.

The technique identifies dynamical objects that organize the transport, and relevant coherent structures. Until recently, the power of these novel Lagrangian approaches has been mainly relegated to mathematical systems or simplified workbench models, since the required detailed knowledge of the velocity field was not readily available in real geophysical situations. However, in the last decades the situation has dramatically changed,

with a rapidly increasing amount of data available from Lagrangian drifters [4], satellite measurements [24], and especially from detailed computer models [25, 26]

2.4 Lagrangian Coherent Structures (LCS) as ridges in the FSLE field

To define a hyperbolic trajectory precisely for systems given only over a finite time-space interval one should be careful, e.g. see [7, 27]. However, let us just think of hyperbolic trajectories as ones about which there is a direction of expansion and a direction of compression. In dynamical systems terminology, this means that there should exist stable and unstable directions about a hyperbolic trajectory. For incompressible flows, without sources or sinks, any expansion in one direction must be balanced by compression in another direction, making such trajectories ubiquitous.

If exponential separation between trajectories occurs, and if the domain of the system is compact, which is typically the case, these trajectories must mix together. This is especially true for turbulent flows, but even for simple dynamical systems this is also true and is often termed ”deterministic chaos”, which refers to the phenomenon that simple vector fields can produce chaotic trajectories. The structures of strongest hyperbolicity often dictate transport in dynamical systems [5], which we will come to see. However, for time-dependent systems these structures, which we refer to as LCS, are often recondite when viewing the Eulerian velocity field or even particle trajectories.
For time-independent systems, separatrices are given by the stable and unstable manifolds of hyperbolic fixed points, as in the pendulum example presented before. However, for highly time-dependent systems, the FSLE fields admit analogous ridges that divide dynamically different regions, and these structures are themselves time-dependent. Notions such as stable or unstable manifolds are well defined for time-independent flows, but for general time-dependent flows, these notions become ambiguous. However, one can loosely think of studying a time-dependent flow in terms of LCS as the analog of studying a time-independent flow in terms of stable and unstable manifolds. Experience dictates that a wide range of systems admit well-defined ridges in the FSLE fields which govern the global flow structure, however we would like to precisely know: Do LCS represent invariant manifolds?
If we refer to LCS as ridges of the FSLE field, we must define a ridge. Intuitively, a ridge is a curve such that if somebody walking along a ridge, then stepping in the direction transverse to the ridge, he would be stepping down. For FTLE, it is known that LCS represent invariant manifolds, and there is mathematical theory for that, but it is not started for FSLE. However we assume that ridges in the FSLE field track the LCS.

2.4.1 LCS properties.

- For well-defined LCS, which are obtained from FSLE field with a sufficient integration time, the flux of matter across such structures is expected to be small.
- The FSLE measures the integrated effect of the flow, so if time is too small then this integrated effect is ignored and thus the FSLE is not very indicative of Lagrangian behavior.
- LCS (at least the ones which are clearly visible in the FSLE fields) are invariant manifolds for all practical purposes.

2.5 Comparison between Eulerian diagnosis and Lagrangian diagnosis from finite-size Lyapunov exponents

As said before, the Eulerian perspective is typically defined as viewing the fluid at fixed points in the domain, perhaps at varying instances in time. When viewing the vector field of a dynamical system, this is the standard perspective. On the other hand, the Lagrangian perspective views the flow in terms of particle trajectories. While the FSLE field is technically a Eulerian field, it is thought of as a Lagrangian quantity since it is computed from particle trajectories.

In contrast with Eulerian diagnostics, Lagrangian tools like the FSLE have the adventage of exploiting both spatial and temporal variability of the velocity field and are in principle able to unveil subgrid filaments generated by chaotic stirring. It was found [18], by comparing with sea-surface temperature patterns, that the two diagnostics provide similar results for slowly evolving eddies like the first Alboran gyre. However, the Lyapunov exponent is also able to predict the (sub-)mesoscale filamentary process. Climatologies of Lyapunov exponents do not show any compact relation with other Eulerian diagnostics, unveiling a different structure even at the basin scale.

Filamentation dynamics can be detected by reprocessing available altimetric or numerical velocity data with Lagrangian tools, giving insight into (sub-)mesoscale stirring processes relevant to tracer observations and complementing traditional Eulerian diagnostics.

2.6 Turbulence and multifractality

In fluid dynamics, [28] turbulence or turbulent flow is a fluid regime characterized by chaotic and stochastic properties. This includes low momentum diffusion, high momentum convection, and rapid variation of pressure and velocity in space and time. Flow that

is not turbulent is called laminar. At very low speeds the flow is laminar, i.e., the flow is smooth (though it may involve vortices on a large scale). As the speed increases, at some point the transition is made to turbulence. In turbulent flow, unsteady vortices appear on many scales and interact with each other. Because laminar-turbulent transition is governed by Reynolds number (that gives a measure of the ratio of inertial forces to viscous forces), the same transition occurs if the size of the object is gradually increased, or the viscosity of the fluid is decreased, or if the density of the fluid is increased.

In the ocean the turbulence causes the formation of eddies of many different length scales. Most of the kinetic energy of the turbulent motion is contained in the large scale structures. In conventional threedimensional turbulence, the energy cascades from the large scale structures to smaller scale structures by an inertial and essentially inviscid mechanism. This process continues, creating smaller and smaller structures which produces a hierarchy of eddies. Eventually this process creates structures that are small enough that molecular diffusion becomes important and viscous dissipation of energy finally takes place. The turbulence in oceanic flow is in two dimensions and the energy cascade is in the inverse direction. There is however a cascade of vorticity towards small scales.

Moreover, the ocean is a system displaying scale invariant behavior. From complex systems theory it is know that fractal sets have an intrinsic scale-invariant nature which can be expressed by a characteristic exponent that is the fractal dimension of the set. There are many definitions of fractal dimension and none of them should be treated as the universal one. The fractal dimension [29] is used to characterize quantitatively a self-similar system. Self-similarity is a symmetry property of the system. By self-similarity we mean invariance under an isotropic transformation, namely a simple dilation. If we consider an object S formed by a set of points $R = (x_1, x_{2,x_3,...})$, a dilation, or similarity transformation with a scaling factor b, changes the coordinates to $bR = (bx_1, bx_{2,bx_3,...})$. The set S formed by the particles of coordinates R is self-similar if it is invariant under this transformation. For a deterministic fractal, scale invariance means that the rescaled system bS is identical with a part of the original system S.
By embedding dimension, d_E, we understand the smallest Euclidean dimension of the space in which a given object can be embedded. The volume $V(l)$ of an arbitrary object can be measured by covering it with balls of linear size l, and volume l^{d_E}. We need $N(l)$ balls to cover it, so

$$V(l) = N(l)l^{d^E}. \tag{2.13}$$

One might at first expect that for any object, $N(l) \sim l^{-d_E}$, since the volume of standard objects does not change with the unit of measurement l. But for fractals we have in general

$$N(l) \sim l^{-D_f}. \tag{2.14}$$

Objects with $D_f < d_E$ are called fractals, with D_f is the fractal dimension. In topological terms, if we have a structure that is a line, the topological dimension is D_f=1, if the structure is a surface D_f=2, and if we have a structure between a line and a surface, we obtain a dimension equals to a fractional number between one and two (fractal dimension).

For a homogeneous fractal, with fractal dimension D_f, many relevant scale-dependent quantities decay as a power law of the scale with exponents which are directly related to the fractal dimension D_f. The widespread occurrence of this behavior led researchers to interpret those systems in terms of fractal sets, and try to characterize universality classes in terms of possible underlying fractal attractors or fractal interfaces.

Nevertheless, a better understanding of the mechanisms that govern the evolution of some dynamical systems, turbulent flows being one of the most relevant cases, evidence that the observed intrinsic complexity could not be covered by a simple description based on the existence of a single fractal interface. As a consequence, a richer framework was required and the natural step forward was to consider multiple-fractal hierarchies which could fit better with the available evidence. Therefore a multifractal system is a generalization of a fractal system in which a single exponent (the fractal dimension) is not enough to describe its dynamics; instead, a continuous spectrum of exponents is needed (See Sect. 4.1).

2.7 Langevin equation and eddy-diffusivity

A stochastic differential equation (SDE) [30] is a differential equation which contains a stochastic process $\xi(t)$:

$$\frac{dx(t)}{dt} = G(x(t), t, \xi(t)) \tag{2.15}$$

where $\xi(t)$ is a stochastic process (random process). As a consequence a SDE is not a single differential equation but rather a family of ordinary differential equations, a different one for each outcome *u* of the stochastic process:

$$\frac{dx_u(t)}{dt} = G(x_u(t), t, \xi_u(t)) \tag{2.16}$$

Therefore, the family of solutions x_u of these differential equations, for different outcomes u, constitute a stochastic process $x(t)$. We can say that to each realization $\xi_u(t)$ of the stochastic process ξ, corresponds a realization x_u of the stochastic process x. The solution x becomes then a functional of the process ξ. To solve a SDE means to characterize completely the stochastic process $x(t)$, i.e. to give the m-times probability density

function (pdf) $f(x1, ..., xm; t1, ..., tm)$. Again, this is in general a rather difficult task and sometimes one focuses only on the evolution of the moments $\langle x(t)^n \rangle$ and the correlation function $\langle x(t_1)x(t_2) \rangle$. When the stochastic process $\xi_u(t)$ appears linearly one talks about a ***Langevin equation***. Its general form being:

$$\frac{dx(t)}{dt} = q(x,t) + g(x,t)\xi(t). \tag{2.17}$$

In this case, $\xi(t)$ is usually referred to as the "noise" term. A word whose origin comes from the random "noise" one can actually hear in electric circuits. Another notation concept: if the function $g(x,t)$ is constant, one talks about additive noise, otherwise, the noise is said to be multiplicative. Finally, *q(x,t)* is usually referred to as the 'drift' term, whereas *g(x,t)* is the 'diffusion' term.

We can use the Langevin equation with additive noise to simulate missing information between points of the grid of the velocity data in the computation of particle's trajectories of the marine flow. In this case x will be the coordinates, $q(x,t)$ is the velocity field and $g(x,t)$ is the diffusion term related to the oceanic diffusivity. Empirical relations between diffusion characteristics were investigated [31] by the use of carefully examined data from instantaneous dye-release experiments in the upper mixed layer of the sea. In this work, among others things, the relation of the variance σ^2 of the initial distribution of path with the diffusion time (time of diffusion during which a patch from a point source grows into the size σ) was studied . The following empirical relation was found:

$$\sigma^2 = 0.0108\, t^{2.34} \tag{2.18}$$

where σ^2 and t are expressed in terms of cm^2 and sec, respectively. The scale of diffusion represents in our case the spatial resolution of the velocity data. The relationship between the diffusivity D_a, in $m^2 s^{-1}$, and the scale of the diffusion, l in m, is given by

$$D_a = 2.055\ 10^{-4} l^{1.15} \tag{2.19}$$

This ocean diffusivity represents the eddy diffusivity, and it depends on the spatial resolution of the FSLE field.

Chapter 3

Lagrangian Coherent Structures (LCS) in marine currents of the Balearic Sea

In this chapter we characterize transport and mixing at meso- and submeso-scale in the area of the Balearic Sea by means of the Finite-Size Lyapunov Exponents, by using velocity data from a numerical model. This technique has already been used to analyze the whole Mediterranean Sea, [16] and the Algerian basin [18].

3.1 Data: Surface velocities in the Mediterranean Sea

In this study and in the studies of the next chapters, we have used data sets from the DieCAST (Dietrich for Center Air Sea Technology) numerical ocean model applied to the Mediterranean Sea with realistic coastlines and topography. The dataset has been already used in previous Lagrangian studies [16, 32, 33]. DieCAST [26] is a primitive equation, z-level, finite difference ocean model using the hydrostatic, incompressible and rigid lid approximations.

Horizontal resolution is the same in both the longitudinal, ϕ, and latitudinal, λ, directions, with resolutions $\Delta_0 = \Delta\,\phi = 1/8^\circ$ and $\Delta\,\lambda = \Delta\,\phi\cos(\lambda)$. Therefore it is important to remark that the original spatial resolution of the velocity field is $\Delta_0 = 1/8^\circ$. Vertical resolution is variable with 30 control volume layers, and the temporal resolution is one day. The thickness of control volumes in the top layer is 10.3 m and they are smoothly increased up to the deepest bottom control volume face at 2750 m. Bathymetry is truncated at 2750 m depth and it is not filtered or smoothed.
The model uses monthly mean wind stress reanalyzed from 10 m wind output from the European Centre for Medium-Range Weather forecasts. Monthly climatology of sea surface temperature and salinity [34] is used to determine the heat and the freshwater sources

in the surface layer that are used to force the model. The only open boundary is the Strait of Gibraltar, where inflow conditions are set similar to observations and outflow is model-determined by upwind. The model is initialized at a state of rest with the annual mean temperature and salinity fields taken from the climatological. Each year is considered to have 12 months, 30 days length each. The climatological forcing we use is adequate to identify the mechanisms and processes occurring under typical or average circumstances. Under this approach, high frequency motions are weak in our model and a daily sampling is adequate. The impact on transport of disturbances containing high frequencies, such as storms or wind burst, is not the focus of the present study and would need specific modelling beyond climatological forcing.

We focus on velocity fields obtained at the second layer, which is localized at depth of 16 m. This is representative of the surface circulation and is not directly driven by wind as the top layer. We have recorded daily velocities for five years, and concentrate our work in the area of the Balearic Sea. The two-dimensional horizontal velocity field on this layer is not exactly incompressible, but it is very close to this situation since typical vertical velocities in the ocean are four orders of magnitude smaller than the horizontal ones ($10^{-5}\ vs\ 10^{-1} m/s$). Because of incompressibility, points at which fluid particles diverge horizontally along particular directions receive fluid along other directions, so that the stretching is linked to mixing. On the other hand, within the FSLE method used in this study and presented in the previous sections, to estimate structures at the mesoscale, fluid particle trajectories need to be integrated only while they undergo horizontal displacements of the order of 100 km, i.e., during 1-10 days (see the next section). Estimating an effective or average vertical velocity for this time as the spatial average of the vertical velocity in horizontal regions of that size, one obtains an effective vertical velocity of $0.1 - 0.7\ m/day$. Thus, during the time of integration, most particles do not leave the horizontal layer considered. In consequence, restricting the study to horizontal motion on a single model layer is a good description of the full transport processes for the space and time scales relevant to mesoscale processes within the FSLE approach.

Fig. 3.1 shows an example of the output of the model for the velocity field in the second layer (16 m depth) of the Balearic Sea at day 640 (the 10th day of the tenth month -October- of the second year of simulation).

Two well known currents, the Northern Current flowing southwards close to the Spanish coast and the Balearic Current associated with the North Balearic Front and flowing northeastwards North of the Balearics, are observed although significantly deformed by the presence of eddies.

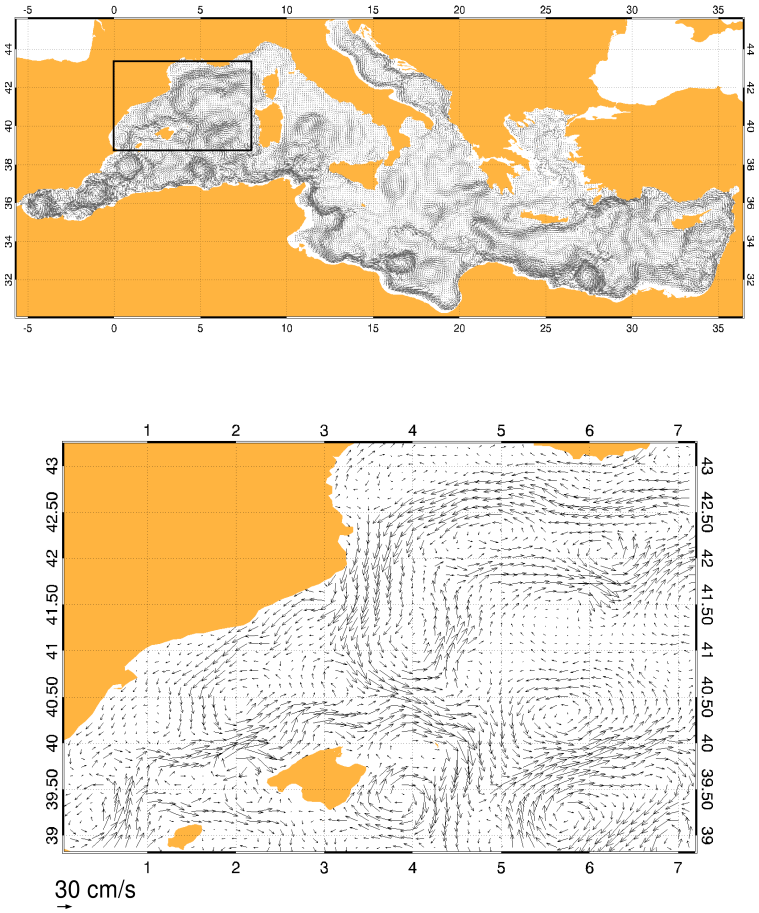

Figure 3.1. Snapshot of the surface velocity field at 16 m depth of the Mediterranean Sea (top) and Balearic Sea (bottom) corresponding to day 640 (October) simulation of the DieCAST model. The Westernmost coast is the Spanish one, the islands are the Balearics. The box inside top figure indicate the area of study.

3.2 Computation of Trajectories and FSLE

As already mentioned, to compute the FSLE (Eq. 2.12) we need to obtain the time, τ, required for two particles of fluid (one of them placed at $\mathbf{x}$) to separate from an initial distance of δ_0 to a final one of δ_f. To compute this time we need to know the trajectories of the particles. The FSLE are computed for the points $\mathbf{x}$ of a lattice with lattice spacing coincident with the initial separation of fluid particles δ_0. The equations of motion that

describe the horizontal evolution of particle trajectories in our velocity field are

$$\frac{d\phi}{dt} = \frac{u(\phi,\lambda,t)}{R\cos\lambda}, \tag{3.1}$$

$$\frac{d\lambda}{dt} = \frac{v(\phi,\lambda,t)}{R}, \tag{3.2}$$

where u and v represent the eastwards and northwards components of the surface velocity field coming from the simulations described in the previous section; R, is the radius of the Earth (6400 km in our computations), ϕ is longitude and λ latitude. Numerically we proceed integrating Eqs. (3.1) and (3.2) using a standard, fourth-order Runge-Kutta scheme, (see Appendix A), with an integration time step $dt = 6$ hours. Since information is provided just in a discrete space-time grid, spatiotemporal interpolation of the velocity data is achieved by bilingual interpolation (see Appendix B). However we notice that bilinear interpolation requires an equally space grid. Our data input is expressed in spherical coordinates, and the grid is not uniformly spaced in the latitude coordinate. In order to interpolate in an uniformly spaced grid, we transform our coordinate system (λ,ϕ) to a new coordinate system with coordinates (μ,ϕ), where the grid turns out to be uniform [33]. The latitude λ is related to the new coordinate μ by

$$\mu = \log|\sec\lambda + \tan\lambda|. \tag{3.3}$$

In the new variables the equations of motion are:

$$\frac{d\phi}{dt} = \frac{u(\phi,\mu,t)}{R\cos\lambda(\mu)} \tag{3.4}$$

$$\frac{d\mu}{dt} = \frac{v(\phi,\mu,t)}{R\cos\lambda(\mu)}, \tag{3.5}$$

and one can convert the μ values back to latitudes λ by inverting Eq.(3.3):

$$\lambda = \pi/2 - 2\arctan(e^{-\mu}). \tag{3.6}$$

Once trajectories are integrated from these equations, one can convert μ values to λ by using Eq.(3.6). Once we integrate the equations of motion, Eqs.(3.4, 3.5), we compute the FSLEs with Eq. (2.12) for the points $\mathbf{x}$ of a lattice with spacing δ_0. Initial conditions for which the prescribed final separation δ_f has not been reached after using all the available times in the DieCAST simulation are assigned a value $\Lambda = 0$. The largest Lyapunov values concentrate along characteristic lines which are manifolds of the most relevant hyperbolic points [11, 16, 18].

3.3 Lagrangian diagnosis

The FSLE has been introduced in order to study non-asymptotic dispersion processes, and for detecting and visualizing Lagrangian structures (e.g., transport barriers or vortex boundaries). In this section we will focus mainly in the second use, and we will also use measures of dispersion and mixing based on the Lagrangian structures detected. The FSLE is inversely proportional to the time at which two particles reach a prescribed separation. In order to characterize the strongest separation (and the fastest convergence along the complementary direction), Λ, is selected as the maximum among the four values obtained when the initial separation δ_0 is chosen along four orthogonal directions.
The field of FSLEs depends on the choice of two length scales: the initial separation δ_0 and the final one δ_f. As in previous works [16, 18] we want to focus here on mesoscale transport. Thus the final length scale, δ_f, is fixed to one degree, i.e., separations of about 110 km at Balearic Sea latitude, which is a typical mesoscale structure size. On the other hand, the smallest scale δ_0 determines the spatial resolution of the FSLE field. In this way the FSLE represents the inverse time scale for mixing up fluid parcels between length scales δ_0 and δ_f. In the first part of this section, we are interested in the spatial distribution of FSLEs, and thus we calculate them at points **x** located on a grid of spacing Δx = δ_0 . A very important fact is that the resolution of the FSLE field can be finer than that of the velocity data, which enables to study submesoscale processes under the typical mesoscales (below 10 kilometers) that nowdays provide altimetry data. This scaling property will be analyzed in the next chapters.

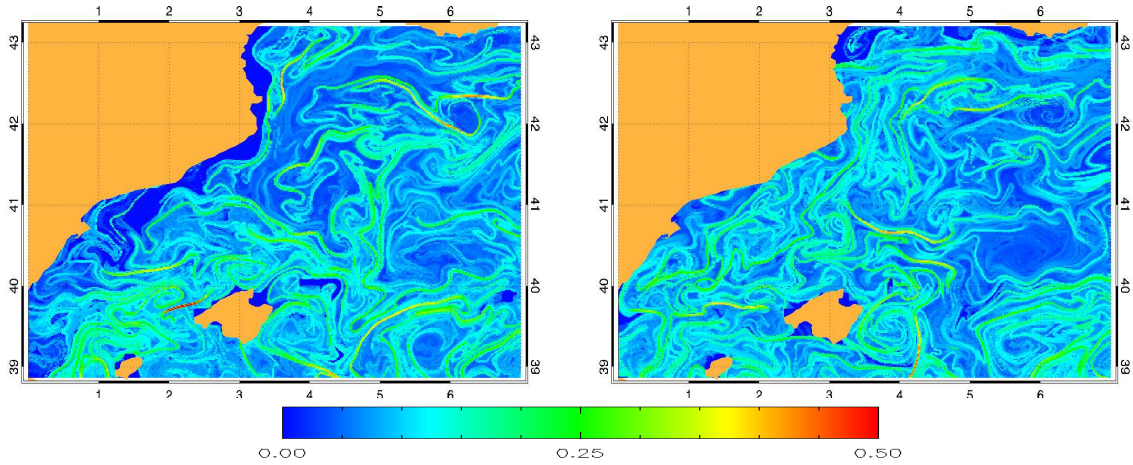

Figure 3.2. Snapshot of spatial distributions of FSLEs backward (left panel) and forward (right panel) in time starting from simulation day 640 (October) of the DieCAST model for the Balearic Sea at resolution $\delta_0 = 1/64°$. Mesoscale structures and vortices can be clearly seen. In both of them we take $\delta_f = 1°$. The colorbar has units of day^{-1}.

We can compute the FSLEs in two ways (Fig. 3.2): from trajectory integration *forwards* and *backwards* in time. Maximum in the spatial distribution of backward FSLEs

identify lines of maximum compression, approximating attracting material lines or unstable manifolds of hyperbolic moving points [11,16]. As observed in others works, forward FSLE maximum values of the spatial distribution organize in lines [11, 12, 16] that provide good approximation to repelling material lines (which are in turn stable manifolds of hyperbolic moving points). Typical values are in the order of 0.1-0.6 $days^{-1}$ corresponding to mixing times for mesoscale distance of 1.7-10 $days$. Since stable and unstable manifolds cannot be crossed by particle trajectories, such lines strongly constrain and determine fluid motion. These lines organize the transport processes in the Sea surface. Spatial structures ranging from the small scales to the ones typical of mesoscale vortices are clearly identified. In the core of the eddies one has low values of FSLEs (i.e., low dispersion rates); on the contrary, the largest values of the FSLE can be found in the outer part of the eddies, where the stretching of the fluid parcels is particularly important, and in lines indicating robust transport barriers.
An important fact, is that in some regions of the vortex cores, chaotic tangles are still observed as local maximum of the FSLE distribution. These maximum are, however, not strong. In fact, even if the stretching is locally very high, the requirement for two points to diverge for more than δ_f =110 km gives a low value of λ to such finer structures.
Since stable and unstable manifolds cannot be crossed by particle trajectories, such lines strongly constrain and determine fluid motion.
Calculating in this way the FSLEs in the region of the Balearic Sea, we unveil the tangle of stretching and compressing lines in which vortices are embedded (Fig. 3.3). As mentioned, these lines also define the directions of transport. Lobes arising from intersections of stretching and compressing lines at a vortex edge indicate where transport in and from the vortex place, whereas tangencies among them provide barriers to transport. In Fig. 3.3 some intersections of stretching and compressing lines are indicated as black dots. These identify Lagrangian hyperbolic points (and their motion define hyperbolic trajectories). Such points correspond to areas with strong mixing activity: fluid is advected here along a compression line and then dispersed away along the stretching line.

This dynamical picture suggests a quantitative measure [16] of mixing in a prescribed area: $M_{\pm}(t) = \left\langle \sqrt{\Lambda_+ \Lambda_-} \right\rangle$, where Λ_+ and Λ_- are the FSLEs in the forward and in the backwards time direction, and the average is the spatial average over the area A. This quantity is large only where hyperbolic points are present. The time dependence of this quantity when the area is the Balearic Sea is shown in the Figure 3.4, characterizing the seasonal variations of mixing. Maximum values, of the order of 0.17 $days^{-1}$, are reached in the beginning of Spring, and minimum values around the beginning of Autumn. Because of the approximate incompressible character of the horizontal flow, the temporal variations of forward and backward FSLEs are strongly correlated, and one expects that the same information can be obtained from just one of the FSLE. Thus one can use a simpler measure of mixing in an area as $M_+(t) = \langle \Lambda_+ \rangle$ or $M_-(t) = \langle \Lambda_- \rangle$. We show in Figure 3.4 that, as expected ([16]), it contains essentially the same information as $M_{\pm}(t)$,

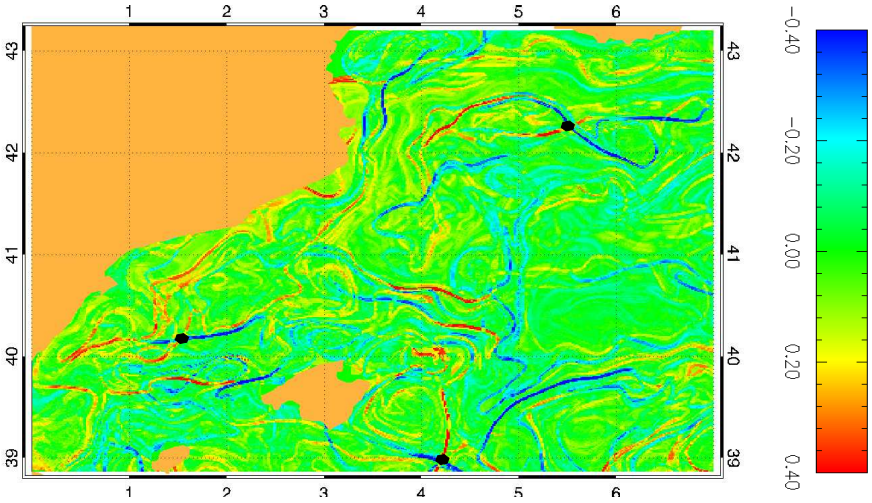

Figure 3.3. FSLEs calculated from forward (displayed as positive values) and backwards (displayed as negative values) integrations in time starting from day 640 (October) of the DieCAST model, i.e., what is plotted is the field $\Lambda_+ - \Lambda_-$ at resolutions of $\delta_0 = 1/64°$. A region with strong mixing appears organized by a tangle of stretching and compressing manifolds. Such lines organize the flow. The black points indicate some of the hyperbolic points that are localized at the intersections of the lines. We take $\delta_f = 1°$. The colorbar has units of day^{-1}.

but it could be measured from floater experiments. It is thus a good characterization of mixing strength. We compare in Fig. 3.5 the temporal behavior of mixing in the Balearic Sea with the whole Mediterranean Sea. This plot shows that the Balearic Sea is an area with strong mixing activity in the Mediterranean Sea in the Spring and Summer seasons.

Computing such a picture for every day of the year and taking the time average, one can obtain a map of regions in the Balearic with different mixing activity (Fig. 3.6) . As expected, the Southern part of the Balearic Sea appears more active, especially in the eastern part. As a further example we compare (Fig. 3.7) the temporal behavior of $M_+(t)$ in the two regions (the North and South of the Balearic Sea) where we expect, from Figure 3.6, to see a very different mixing activity. The South area presents more mixing activity than the North area probably because of the influence of the Algerian current. In addition, the two areas show seasonal fluctuations but the timing in the mixing processes are diferent, when one of them reaches a local maximum the other one reaches a local minimum.

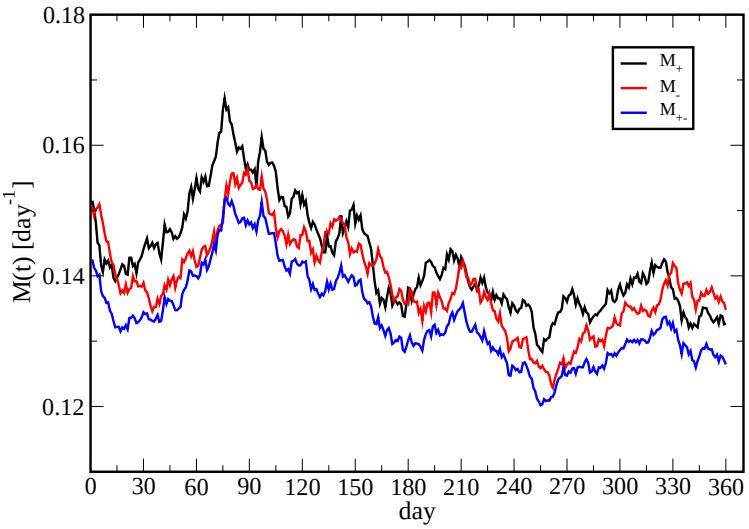

Figure 3.4. Temporal evolution of the mixing measures $M_{\pm}(t)$ and $M_{+}(t)$ for the Balearic Sea during one simulation year. They display a similar behavior with maximun values in March, and minimum value in September.

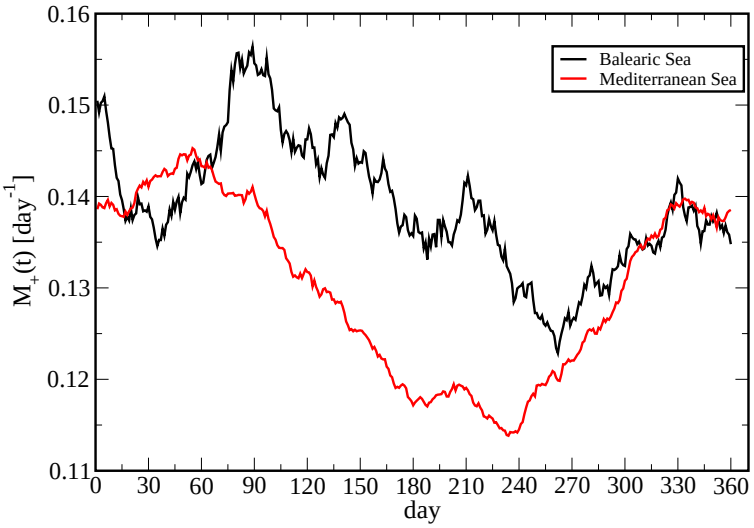

Figure 3.5. $M_{+}(t)$ during one year for the Balearic Sea and the Mediterranean Sea. The figure show the same seasonal behavior but different values in magnitude in Spring and Summer.

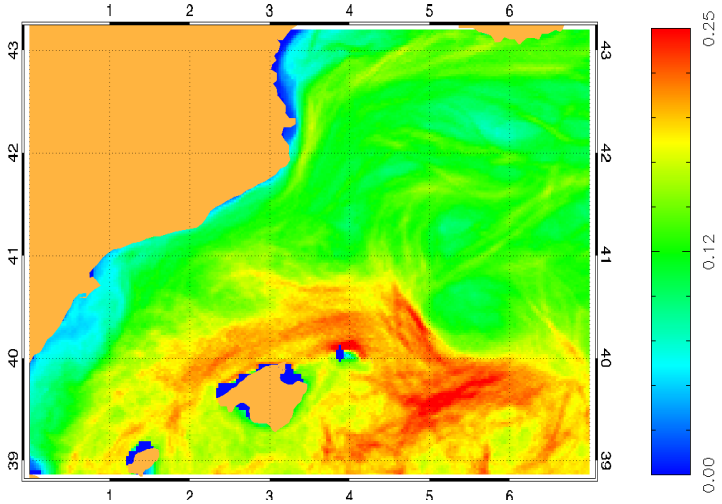

Figure 3.6. Time average (for the second simulation year) of the FSLEs in the Balearic Sea. Geographical regions of different mixing activity appear. The colorbar has units of day^{-1}.

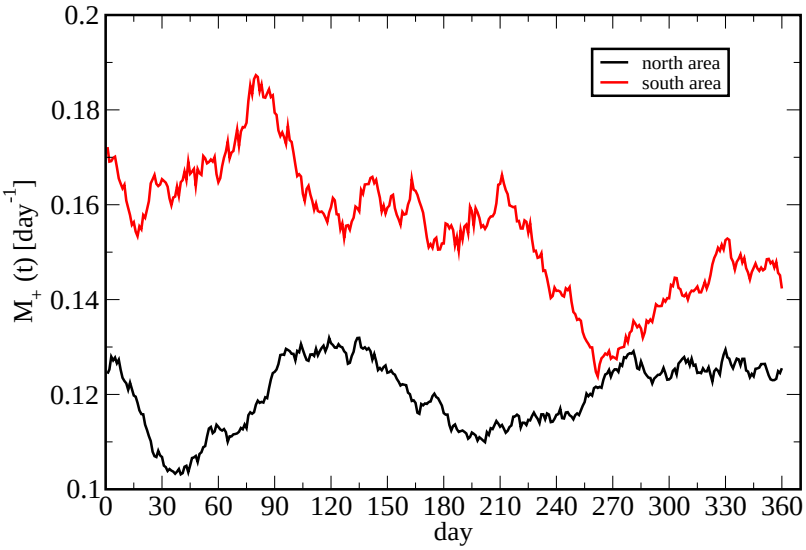

Figure 3.7. Temporal evolution of the mixing measures $M_+(t)$ for the North and South area of the Balearic Sea during one simulation year. They display a seasonal behavior but different in magnitude.

Chapter 4

Scale invariance properties of FSLE

A very important fact is that the resolution of the FSLEs field can be finer than that of the velocity data. This enables to study submesoscale processes under the typical mesoscales, below 10 kilometers, that are the standard sizes of numerical models or of altimetric data. This is subject to some controversy since one needs to interpolate the velocity to a grid of resolution δ_0, smaller than the resolution of the initial velocity data and this could induce some artificiality in the results. A way to account to this question is to analyze the multifractal properties of the FSLEs. If they show it then they do not have a characteristic spatial length and are somehow repeated at every scale. Thus the FSLE properties under the subgrid scale should be as valid as the ones above. On the other side, Lyapunov exponents at infinite time have a multifractal structure and the FTLE distribution is known to reflect this scaling behavior when $T \to \infty$ [35]. But no similar theory has been developed for FSLE. We expect to observe the same multifractal scaling when $\delta_0 \to 0$, and this will be checked in the first section of this chapter.

Another related question is what happens when there is a loss in the resolution of the velocity field: Do we obtain the same LCS?. We analyze this question in the second part of the chapter.

4.1 FSLE at different spatial scales

In our computation of the FSLE field, beside $\delta_0 = 1/8°$, which is the DieCAST grid resolution, we will use $\delta_0 = 1/16°, 1/32°, 1/64°$.

In Figure 4.1 we plot the FSLE field for the same day computed at different resolutions. As the resolution gets finer (smaller δ_0) more dynamical structures are revealed and filaments gets thinner, with typical widths much smaller that the 10 kilometers of the velocity data resolution. This is the reason for the claim that FSLEs provide information below data resolution length-scale. It is remarkable, however, that the large-scale structures are not much affected by the changing resolution: they are just sharper or more blurred, but maintaining the same shape and locations. We next compute the probability

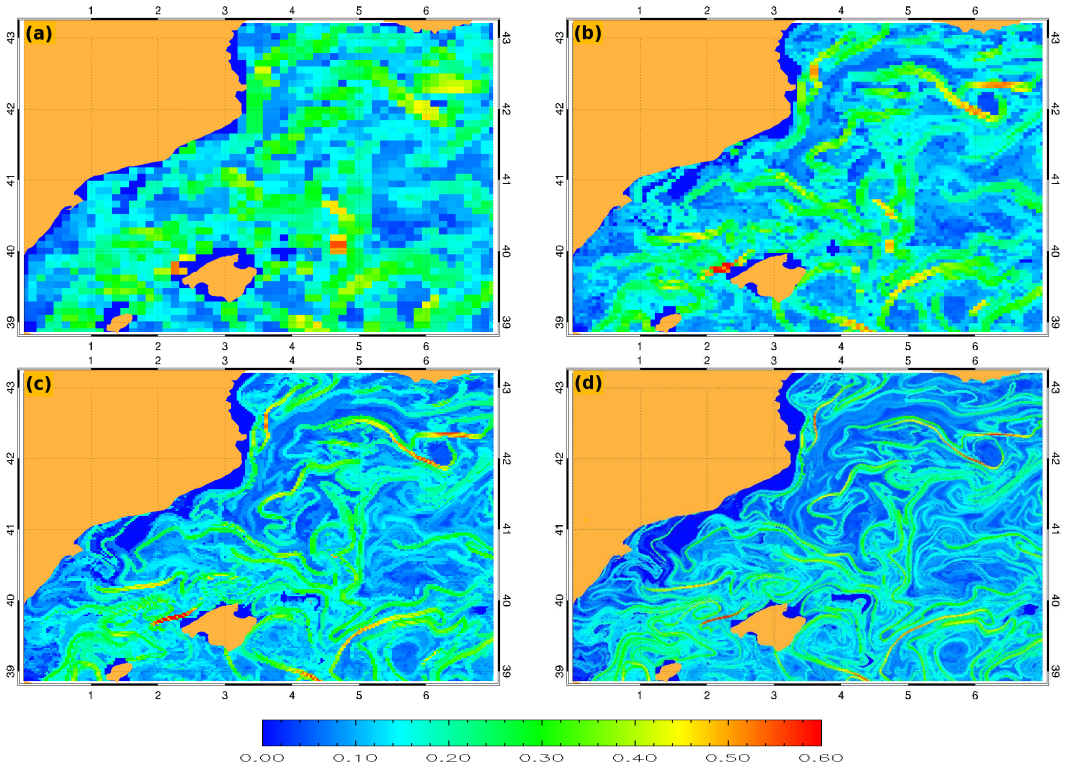

Figure 4.1. Snapshots of spatial distributions of backward FSLEs, starting from day 640 of the DieCAST model at different resolutions: a)$\delta_0 = 1/8°$, b) $\delta_0 = 1/16°$, c) $\delta_0 = 1/32°$, d) $\delta_0 = 1/64°$. In all of them we take $\delta_f = 1°$. The numbers in the color bar have units of day^{-1}. Initial conditions for which the separation δ_f has not been reached after 640 days are assigned a value $\Lambda = 0$.

density distribution of the FSLE, $P(\delta_0, \Lambda)$, for different resolutions δ_0. In Fig. 4.2 we show the histograms (averaged over 30 snapshots distributed among 15 months) normalized to the same unitary area. One can see that when the resolution gets finer the $P(\delta_0, \Lambda)$ narrows, and the peak height increases. Despite the probability density concentrates close to a mean value (say $\overline{\Lambda} \approx 0.1$), large deviations remain even for relatively high resolution.

The way the structures in Figure 4.1 and the corresponding histograms in Figure 4.2 change with changing resolution suggests a multifractal character for the FSLE field, different scaling hapens in different points, which organize in manifolds with a particular dimension. To check this we propose the relationship [36]:

$$P(\delta_0, \Lambda) = P(\delta_0, \Lambda_c)\, \delta_0^{d-D(\Lambda)}, \tag{4.1}$$

where $P(\delta_0, \Lambda_c)$ is the maximum value of P at a given resolution scale δ_0, d is the dimension of the embedding space ($d = 2$ in our case), and thus $D(\Lambda)$ is the fractal dimension of the set of points having FSLE with the value Λ. From Eq.(4.1) one has

$$D(\Lambda) = d - \frac{\log \frac{P(\delta_0,\Lambda)}{P(\delta_0,\Lambda_c)}}{\log \delta_0}. \tag{4.2}$$

The plot of $D(\Lambda)$ in Figure 4.2 (right) shows a collapse at different scales confirming the hypothesis in Eq.(4.1). (The collapse is not perfect due to the lost of translational invariance produced by the small size of the domain -the Balearic basin- that we analyze, as well as to the presence of coasts). Thus, the interfaces of constant Λ values build a multifractal hierarchy and generalized scale invariance is present in the FSLE field.

Maximum values in the histograms (Top figure in Fig. 4.2) are the most probable FSLE values. These FSLE values have a fractal dimension equal to two (bottom figure in Fig. 4.2), therefore in the greater part of the FSLE field you find structures of dimension two. The fractal dimension of the regions with larger values of Λ is close to one, and since objects with dimension one are lines, the ridges of FSLE are located along lines.

4.2 FSLE at different spatial resolution of the velocity field

As was said the resolution of the velocity field in the DieCAST model is $\Delta_0 = 1/8^\circ$. To simulate a resolution loss we replace each square in the grid made by four points by a single point, with the velocity there being the average of the four points. In this way we reduce the velocity resolution to $\Delta_0 = 1/4^\circ$. We repeat again the procedure to obtain a new velocity field with a still coarser resolution of $\Delta_0 = 1/2^\circ$. The velocity field at these new resolutions are plotted in figure 4.3, and the FSLE computed using these new velocity fields are shown in figure 4.4.

It is clear that the FSLEs fields obtained from lower resolution velocity fields have a smoother structure, with smaller horizontal mesoscale structures suppressed (the sub-mesoscale filamentary structure, however, remains, since its size is controlled by δ_0). A pointwise comparison of the fields obtained at the nominal DieCAST resolution and the coarser ones gives large errors. However, the main large-scale structures and the lines with the strongest values of Λ, the LCSs, are not greatly changed.

Fig. 4.5 displays the relative error $< \epsilon(t) >$ of the FSLEs with respect to the ones calculated for the original resolution $\Delta_0 = 1/8^\circ$. $< \epsilon(t) >$ is obtained from the following formulas:

$$\epsilon(t_i) = \sqrt{\frac{1}{N}\sum_{\mathbf{x}} \frac{|\Lambda^\alpha(\mathbf{x},t_i) - \Lambda(\mathbf{x},t_i)|^2}{|\Lambda(\mathbf{x},t_i)|^2}}, \quad < \epsilon(t) > \equiv \frac{1}{s}\sum_{i=1}^{s} \epsilon(t_i)\ . \tag{4.3}$$

with Λ^α is the Lyapunov field corresponding to coarser values of Δ_0, and Λ is the Lyapunov field at original spatial resolution of the velocity field. The sum over points $\mathbf{x}$ is restricted to the places where $\Lambda(\mathbf{x},t) > 0.2$, and each panel of the figure is for the two spatial resolutions of the FSLE field $\delta_0 = 1/8^\circ$ and $\delta_0 = 1/64^\circ$. The relative error is large in both cases. However, it is important to note that this is due to the fact that the new resolution of the velocity field ($\Delta_0 = 1/2^\circ$) is much larger than the original one

($\Delta_0 = 1/8°$). That is, almost a difference of $40km$ in the velocity spatial resolution. Finally, To get an idea of how relevant these quantities are, we have computed the relative error of shuffled FSLEs with respect to the original field, and obtained the values 1.143 and 1.292 for $\delta_0 = 1/8°$ and $\delta_0 = 1/64°$, respectively, and at $\Delta_0 = 1/8°$. The shuffling procedure consists in generating Lyapunov maps by doing a random permutation of the original values of FSLE in space and time. This keeps invariant the FSLE histograms, but destroys any spatial and temporal correlation.

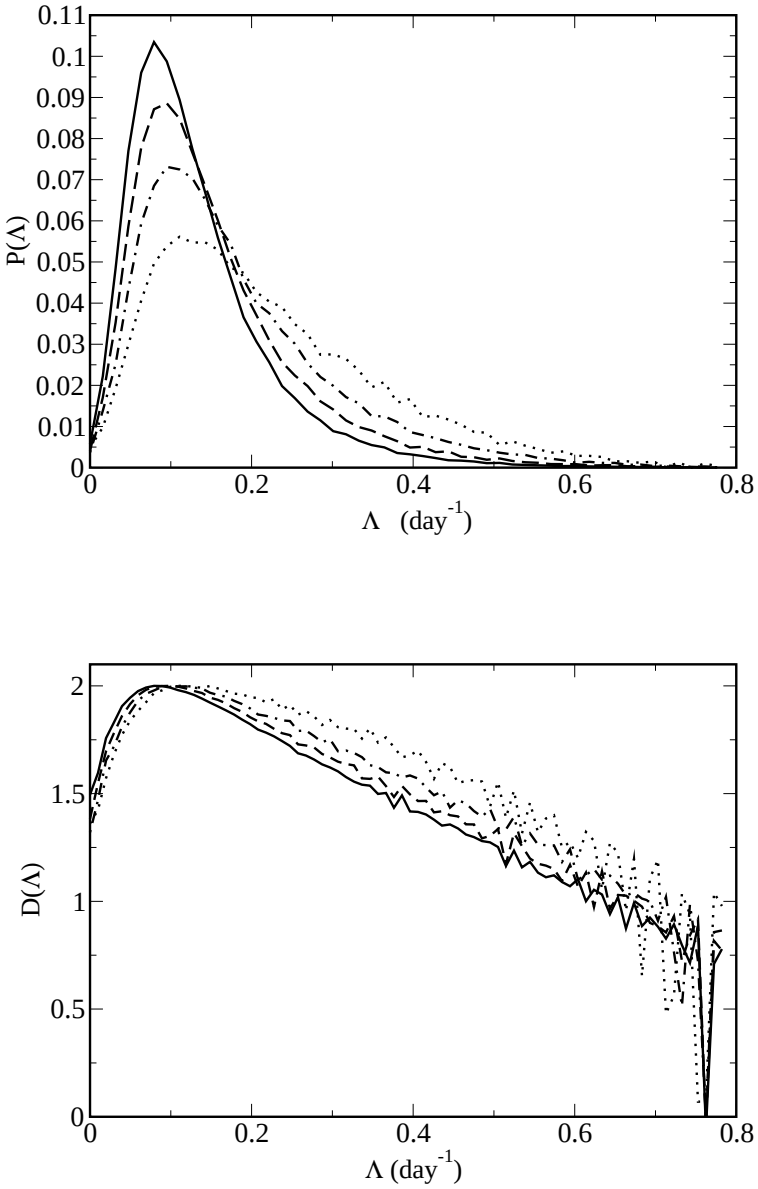

Figure 4.2. Top: Comparison of the probability density functions $P(\delta_0, \Lambda)$ for the FSLEs at different resolutions. It is obtained from the temporal average (30 snapshots) of instantaneous histograms of λ. Dotted line is for $\delta_0 = 1/8°$, dashed-dotted line $\delta_0 = 1/16°$, dashed $\delta_0 = 1/32°$, and solid line for $\delta_0 = 1/64°$. Bottom: $D(\Lambda)$ calculated from Eq. (4.2) for different values of δ_0. Dotted for $\delta_0 = 1/8°$, dashed-dotted line $\delta_0 = 1/16°$, dashed $\delta_0 = 1/32°$, and solid line line for $\delta_0 = 1/64°$.

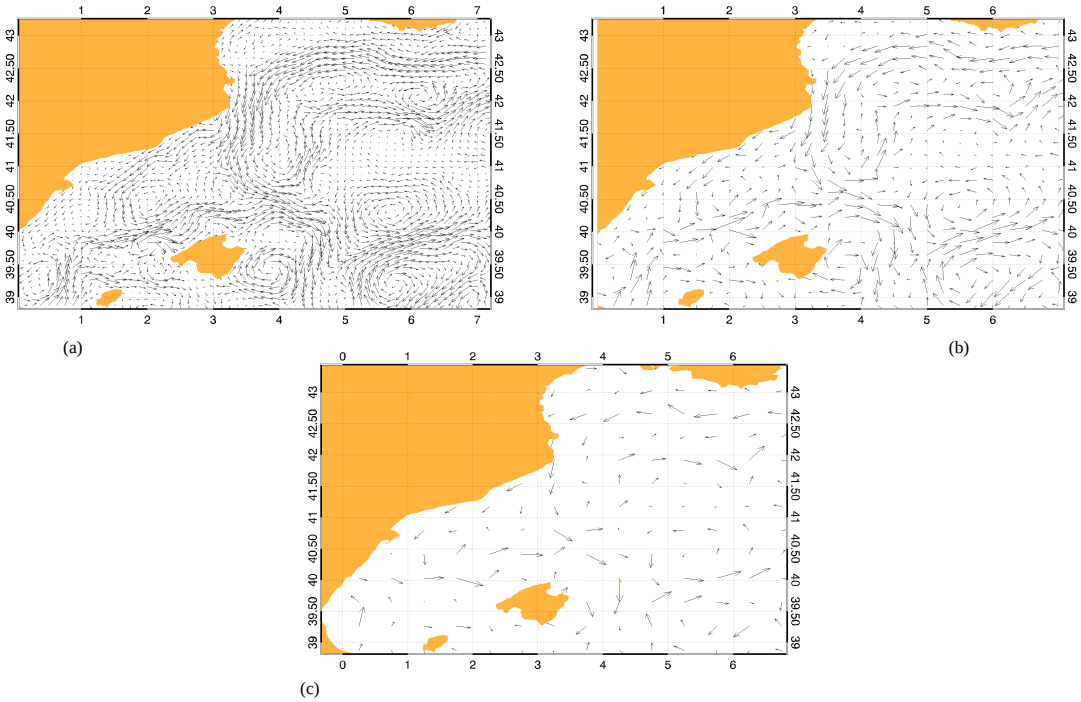

Figure 4.3. Snapshots of velocity fields for the day 640 of the DieCAST model at different resolutions a) $\Delta_0 = 1/8°$, b) $\Delta_0 = 1/4°$, c) $\Delta_0 = 1/2°$.

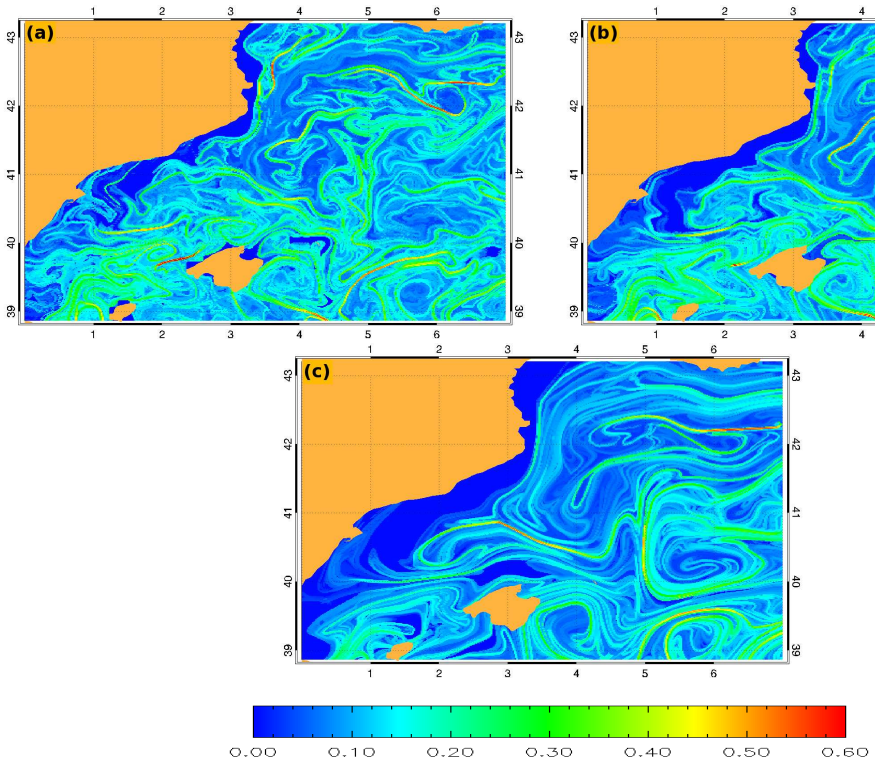

Figure 4.4. Snapshots of FSLEs calculated backwards in time starting from day 640 of the DieCAST model at different resolutions of the velocity field: a) $\Delta_0 = 1/8°$, b) $\Delta_0 = 1/4°$, c) $\Delta_0 = 1/2°$. In all of them $\delta_0 = 1/64°$. The color bar has units of day^{-1}. Initial conditions for which the separation δ_f has not been reached after 640 days are assigned a value $\Lambda = 0$.

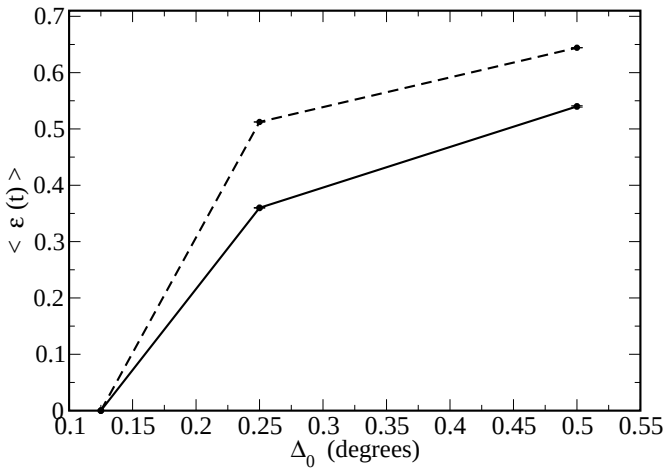

Figure 4.5. Relative error $< \epsilon(t) >$ of the FLSE fields at different values of velocity resolution (Δ_0) with respect to the nominal case $\Delta_0 = 1/8^\circ = 0.125^\circ$ (only the points at which the Lyapunov field at this nominal resolution exceed 0.2 are considered). Spatial resolution is $\delta_0 = 1/8^\circ$ (solid line) and $\delta_0 = 1/64^\circ$ (dotted line). $< \epsilon(t) >$ is obtained by temporally averaging the error in 100 snapshots. Only The error bar indicates the statistical error of the $< \epsilon(t) >$ average. $\delta_f = 1^\circ$.

Chapter 5

Robustness of FSLEs

Numerical, satellite or in-situ obtained oceanic surface velocity fields are subjected to many different sources of error. Numerical models are mainly plagued by errors coming from the finite scale resolution, uncertainty in the boundary and external forcing conditions, and in the numerical algorithm itself. On the other hand, altimetry-based velocity errors are due to orbit configuration, estimation methods, smoothing, atmospheric corrections, calculation of the mean flow from the geoid, interpolation of satellite tracks to grid points, etc. Typical errors for in-situ data are of instrumental origin and human manipulation, but also due to the interpolation of tracks to a grid, atmospheric conditions and many others. It is therefore natural to ask how the *error* in the velocity field translates into the FSLE computation. In addition one may consider the influence of uncertainties in the computation of fluid particle trajectories due to unresolved small scales. In this chapter we consider these: first the role of errors in velocity, and finally the role of the error in the trajectories.

5.1 Error in the data

We compute the FSLEs after applying a random perturbation to all components of the velocity field. The velocity is changed from (u, v) to (u', v'), with $u'(\mathbf{x}, t) = u(\mathbf{x}, t)(1 + \alpha\eta_x(\mathbf{x}, t))$ and $v'(\mathbf{x}, t) = v(\mathbf{x}, t)(1 + \alpha\eta_y(\mathbf{x}, t))$. $\{\eta_x(\mathbf{x}, t), \eta_y(\mathbf{x}, t)\}$ are sets of Gaussian random numbers of zero mean and unit variance. α measures the relative size of the perturbation. We introduce three different kinds of error: uncorrelated noise, i.e. different and uncorrelated values of $\{\eta_x(\mathbf{x}, t), \eta_y(\mathbf{x}, t)\}$ for each $\mathbf{x}$ and t; correlated in time and uncorrelated in space (uncorrelated for different $\mathbf{x}$ but the same values at given $\mathbf{x}$ for different t); and correlated in space and uncorrelated in time (uncorrelated values for different t, but the same values for different $\mathbf{x}$ at fixed t). Note that the perturbation is proportional to the original velocity.

Fig. 5.1 shows snapshots of FSLEs at the same time for different values of $\alpha = 0, 20, 60, 100$, for the case of perturbation uncorrelated in time and in space. The com-

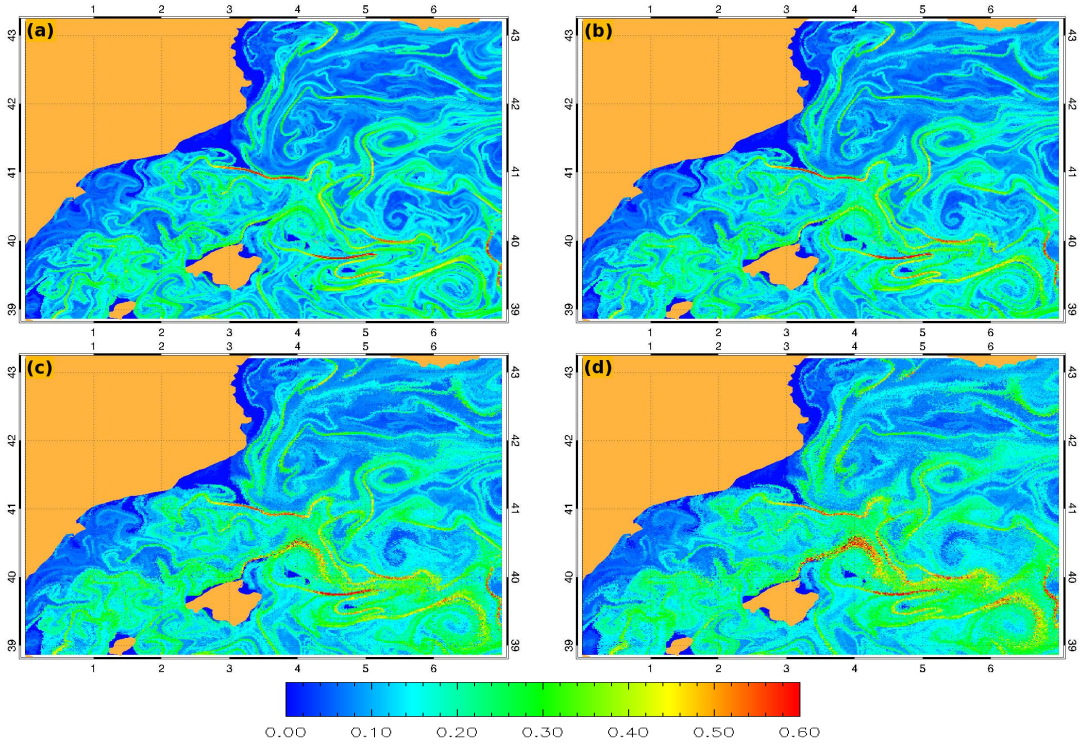

Figure 5.1. Snapshots of FSLEs calculated backwards in time starting from day 600 of the DieCAST simulation at fixed spatial resolution ($\delta_0 = 1/64°$), and at different α (relative size of the perturbation of velocity, for the case in which it is uncorrelated in space and time): a)α = 0, b) α = 20 , c) α = 60 , d)α = 100 . In all of them we take $\delta_f = 1°$. The color bar has units of day^{-1}. Initial conditions for which the separation δ_f has not been reached after 600 days are assigned a value $\Lambda = 0$.

puted Lagrangian structures look rather the same, despite the large size ($\alpha = 100$ means perturbation 100 times larger than the initial velocity field) of the perturbation introduced.

We quantify the influence of the velocity perturbation in the FSLE calculation by computing the relative error of the perturbed with respect to the unperturbed Lyapunov field at a given instant of time, and then averaging in time (we have $s = 100$ snapshots: $t = t_1, ..., t_s$) from formulas similar to 4.3, but with $\Lambda(\mathbf{x}, t_i)$ and $\Lambda^\alpha(\mathbf{x}, t_i)$ replaced by the FSLEs fields without and with inclusion of the perturbation in the velocity data, respectively. The sum over **x** runs over the $N = 2679$ spatial points. Figure 5.2 displays, as a function of α, the average error $< \epsilon(t) >$.

The important result is that the relative error has always small values: even for $\alpha = 10$ (i.e. a perturbation ten times larger than the initial velocity field) the relative error remains smaller than 0.23 for the three kinds of noise, at the same spatial resolution of velocity data $\Delta_0 = 1/8°$, and at spatial resolution of the FSLE field $\delta_0 = 1/8°$. This result is also obtained at a finer spatial resolution of the FSLE field $\delta_0 = 1/64°$ and at the same spatial resolution of the velocity field $\Delta_0 = 1/8°$, where the relative error is slightly higher than 0.5. The relative errors computed for the shuffled FSLEs take the values 1.14 and 1.3 for

$\delta_0 = 1/8^\circ$ and $\delta_0 = 1/64^\circ$, respectively.

These results confirm that the values and spatial distribution of the FSLEs are robust to relatively large amount of error in the velocity field provided the errors are spatially or temporally uncorrelated. The reason for this is the averaging effect produced when computing FSLEs by integrating over trajectories which extend in time and space, make them rather robust against several types of uncorrelated noise in the velocity data.

5.2 Noise in the particle's trajectories

In section 5.1 we introduced noise in the velocity data to mimic possible uncertainties affecting them, and computed the FSLEs for the resulting fields. Now we proceed seemingly but by adding the noise to the particle trajectories. This is a simplified way of including unresolved small scales in the Lagrangian computations [37]. To be precise we solve numerically (see Appendix C) the following system of equations:

$$\frac{d\phi}{dt} = \frac{u(\phi,\lambda,t)}{R\cos(\lambda)} + \frac{\sqrt{2D}}{R\cos(\lambda)}\xi_1(t), \tag{5.1}$$

$$\frac{d\lambda}{dt} = \frac{v(\phi,\lambda,t)}{R} + \frac{\sqrt{2D}\xi_2(t)}{R}. \tag{5.2}$$

$\xi_i(t)\ \ i = 1, 2$ are the components of a two-dimensional Gaussian white noise with zero mean and correlations $< \xi_i(t)\xi_j(t') >= \delta_{ij}\delta(t - t')$. Eqs. (5.1, 5.2) use a simple white noise added to the trajectories. A more realistic representation of small-scale Lagrangian dispersion in turbulent fields requires using other kinds of correlated noises [37] but, as we are interested in examining influences of the missing scales, it is convenient to use white noise, since this would represent the extreme case of very irregular trajectories which gives an upper bound to the effects of more realistic smoother small scales. Thus the tests presented in this subsection are similar to the ones considered in subsection 5.1 when adding uncorrelated perturbations to the velocity, but here the perturbation acts at arbitrarily small scales, as appropriate for a turbulent field, instead of being smooth below a cutoff scale, as appropriate for modelling observational errors.

For the diffusivity we use Okubo's empirical formula [31], which relates the effective eddy-diffusion, D in m^2/s, with the spatial scale, l in meters: $D(l) = 2.055\ 10^{-4}\ l^{1.15}$. If we take $l = 12\ km$, which is the approximate length corresponding to the $1/8^\circ$ DieCAST resolution at Mediterranean latitudes, we obtain $D \sim 10\ m^2 s^{-1} \equiv D_0$.

First, in Fig. 5.3 we show particle trajectories without (top panel) and with (bottom panel) the eddy diffusion. As expected diffusion modelled by random motion introduces small scale irregularities on the trajectories, but also it introduces substantial dispersion at large scales. In Fig. 5.4 we show snapshots of FSLEs for the same day and at the same spatial resolution $\delta_0 = 1/64^\circ$, but obtained for different values of D. We can see that the

main mesoscale structures are maintained, but the small-scale filamental structure is lost since filaments widen. This is somehow expected a priory because diffusion introduces a new length scale l_D which scales as $\sqrt{D}$. As in Sect. 4.2, pointwise error computations give large values due to the obvious differences between the fields presented in Fig. 5.4. Again it is more relevant to restrict to the LCS locations, which we take as the places where $\Lambda > 0.2$ in the $D = 0$ computation. Left panel of Fig. 5.5 shows the relative error with respect to the $D = 0$ case (computed from formulas analogous to Eq. (4.3)) of the FSLEs obtained at different values of D. The relative error monotonously increases with D, but remains smaller than 0.6 for the largest value of D considered. In the same way than in previous subsections, in order to get an idea of how relevant these relative errors are, we computed the relative error of shuffled FSLE with respect to the original field, and we get a value of 1.143.

A complementary set of numerical experiments are plotted in the right panel of Fig. 5.5. First, with solid line we plot the relative error of FSLE if we consider a fixed eddy diffusivity ($D_0 = 10m^2s^{-1}$), and change the spatial resolution, δ_0. It is observed that the error increases when the spatial resolution δ_0 is finer than the length scale introduced by the eddy-diffusion. Moreover with dotted-line it is plotted the case in which the eddy-diffusion takes the value corresponding to each δ_0 using Okubo's formula (i.e. at $\delta_0 = 1/16^\circ$ $D = 4,5m^2s^{-1}$; at $\delta_0 = 1/32^\circ$ $D = 2m^2s^{-1}$; at $\delta_0 = 1/64^\circ$, $D = 0.9m^2s^{-1}$). Now $< \epsilon(t) >$ takes a constant value close to 0.45. This result shows that if we use a spatial resolution smaller than velocity data resolution, the eddy-diffusion must be the one computed for the corresponding length scale. This constant value somehow corroborates the diffusion Okubo's formula. The dashed-dotted line corresponds to the shuffling experiment, included for comparisons.

A final numerical study (shown in Fig. 5.6) consists in computing the histograms of FSLEs, with and without eddy diffusion, which takes always the same value $D_0 = 10m^2s^{-1}$, for different resolutions. It is seen that for $\delta_0 = 1/8^\circ$ the histograms with and without diffusion are coincident. This is due to the fact that the value of diffusion we are using is the one corresponding, by the Okubo formula, to $1/8^\circ$. I.e., we are parametrizing turbulence below $1/8^\circ$, and this has no effects on the FSLE computations if the minimum scale considered is also $1/8$. However, this behavior is different for larger δ_0 (maintaining the same value $D_0 = 10m^2s^{-1}$). The histograms for $\delta_0 = 1/16, 1/64^\circ$, with and without diffusion, are clearly different. In fact, one finds that histograms at $\delta_0 = 1/64^\circ$ with diffusion turns out to be rather similar to the $\delta_0 = 1/16^\circ$-resolution histogram without diffusion. This somehow confirms the averaging effect over smaller scales that is performed after adding noise to the particle trajectories.

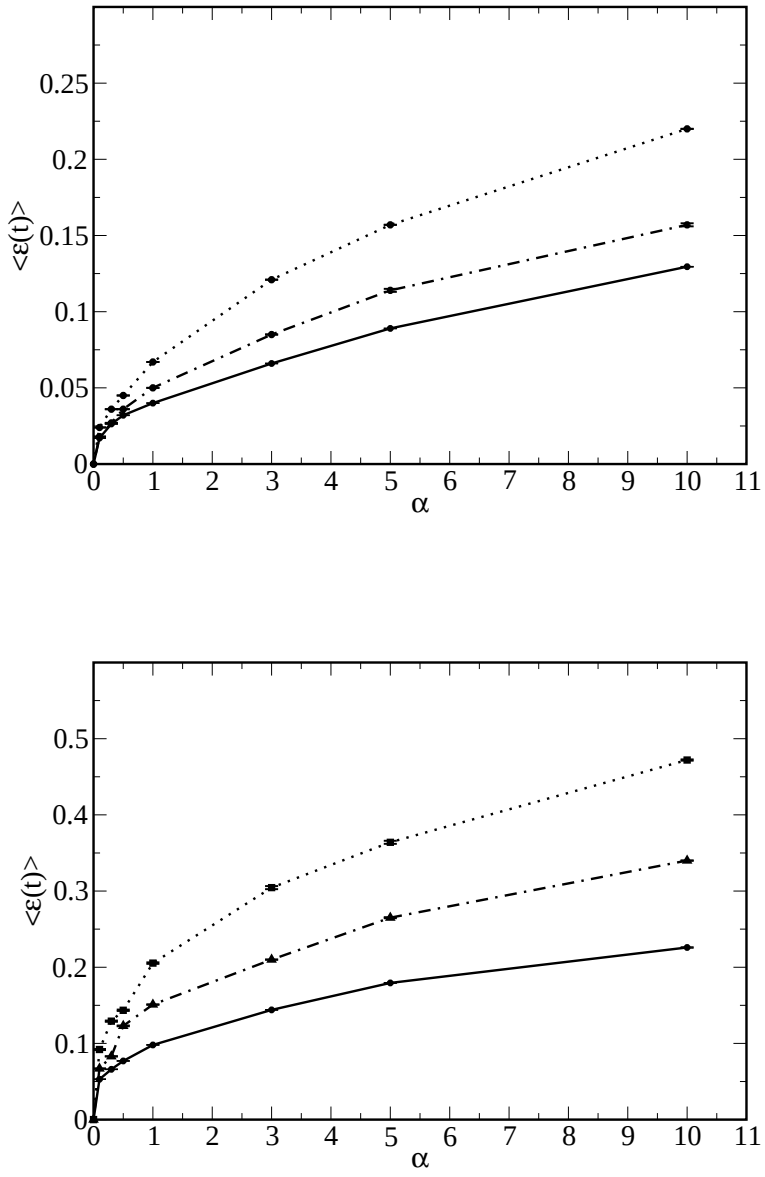

Figure 5.2. Relative error $< \epsilon(t) >$ of the FSLE fields for different perturbation intensity α in the velocity data. Solid line is for uncorrelated noise in space and time, dashed-dotted line is for uncorrelated noise in time and correlated in time, and dotted line is for uncorrelated noise in space and correlated in time. $< \epsilon(t) >$ is obtained by averaging the relative error in 100 snapshots (see Eq. (4.3)). The error bar is the statistical error of the temporal average $< \epsilon(t) >$. Top: spatial resolution $\delta_0 = 1/8°$. Bottom: spatial resolution $\delta_0 = 1/64°$. In all calculations we take $\delta_f = 1°$

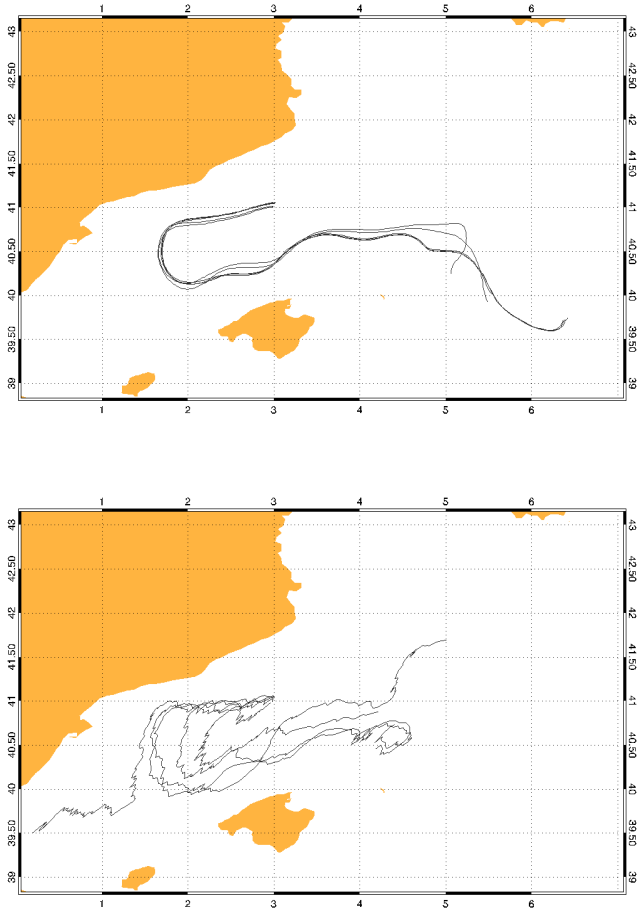

Figure 5.3. Trajectories of five particles without diffusion (top) and with diffusion (bottom). The difference in the initial positions of all five particles is about $0.06°$, and we use these initial conditions in both computations. These trajectories were computed for 50 days of integration. We used the eddy-diffusion $D_0 \sim 10m^2s^{-1}$ assigned by the Okubo formula to the resolution of the DieCAST model at Mediterranean latitudes.

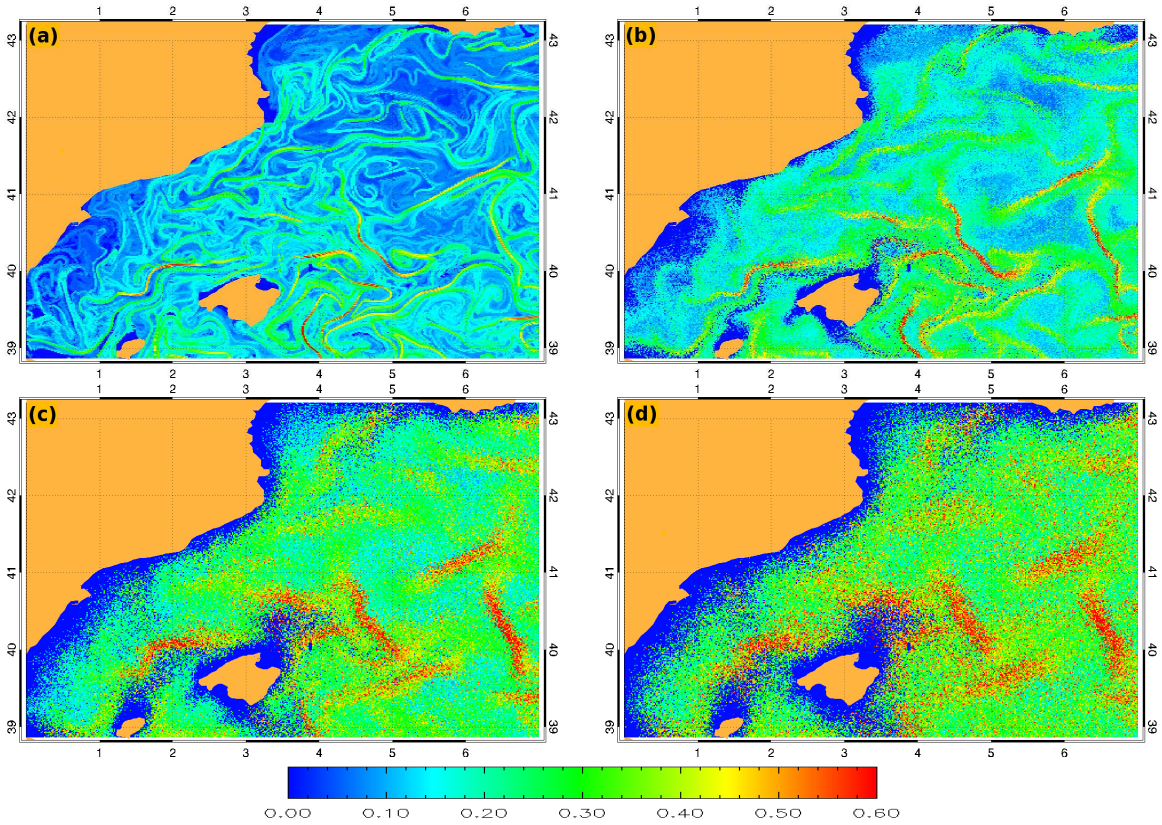

Figure 5.4. FSLEs computed backwards from day 500 of the DieCAST model, at the same spatial resolution ($\delta_0 = 1/64°$), and for different eddy-diffusion values: a)$D = 0\ m^2 s^{-1}$ b) $D = 0.9\ m^2 s^{-1}$, c)$D = D_0 = 10\ m^2 s^{-1}$, d)$D = 17\ m^2 s^{-1}$. In all of them we take $\delta_f = 1°$. The color bar has units of day^{-1}. Initial conditions for which the separation δ_f has not been reached after 500 days are assigned a value $\Lambda = 0$.

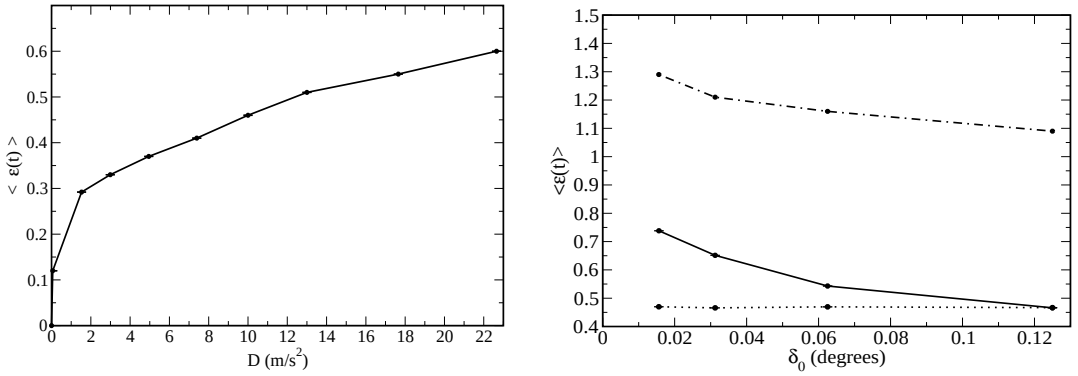

Figure 5.5. Left: Relative error $< \epsilon(t) >$ of the FSLE at the different values of D in the particle trajectories, with respect to the $D = 0$ case. Spatial resolution is $\delta_0 = 1/8°$, and $\delta_f = 1°$. $< \epsilon(t) >$ is obtained by temporally averaging the relative errors in 100 snapshots. The (small) error bars indicates the statistical error in the $< \epsilon(t) >$ average. Right: Dotted line is the relative error $< \epsilon(t) >$ of the FSLE at different spatial resolution δ_0 and at the eddy-diffusion D assigned by the Okubo formula to every spatial resolution, with respect to the $D = 0$ case. Solid line is the relative error $< \epsilon(t) >$ of the FSLE at different spatial resolution δ_0, and at the same eddy-diffusion $D_0 = 10m^2s^{-1}$ in the particle trajectories with respect to the $D = 0$ case. Dashed-dotted line is the relative error of shuffled FSLE with respect to the original case ($D = 0$) at different spatial resolution. $< \epsilon(t) >$ by temporally averaging the relative error in 100 snapshots. The (small) error bar indicates the statistical error in the $< \epsilon(t) >$ average. In all of them we take $\delta_f = 1°$.

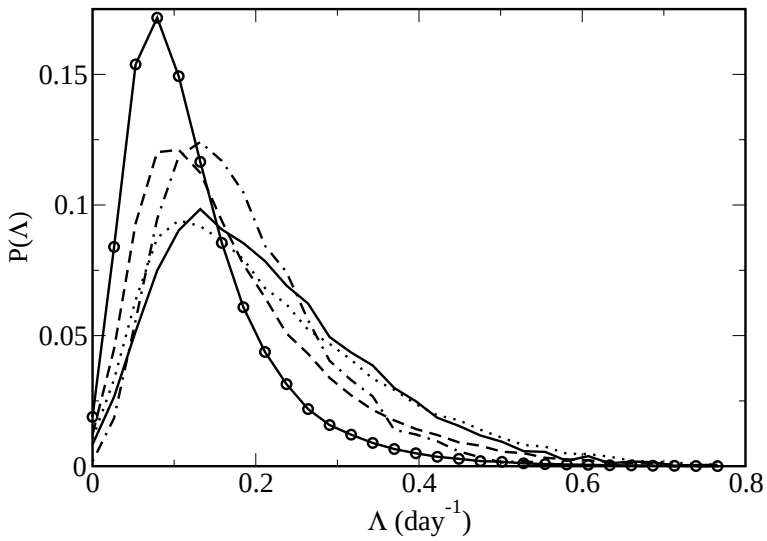

Figure 5.6. Comparison between probability density function for the FSLEs at different resolutions with eddy-diffusion, and without diffusion. It is obtained from the temporal average (30 snapshots) of histograms. Solid line for $\delta_0 = 1/8°$ at eddy-diffusion $D_0 = 10m^2s^{-1}$, dotted $\delta_0 = 1/8°$ without diffusion, dashed $\delta_0 = 1/16°$ without diffusion, dashed-dotted line for $\delta_0 = 1/64°$ with eddy-diffusion $D_0 = 10m^2s^{-1}$, and circle-line for $\delta_0 = 1/64°$ without diffusion.

Chapter 6

Summary

In this work we have analyzed and quantified, from marine surface velocity fields provided by a numerical model, several statistical properties and robustness of FSLE, in order to study the intermittency and its impact in transport and mixing.

We have increased the spatial resolution of FSLE field improving the identification of Lagrangian Coherent Structures. The spatial distribution of FSLEs display a scale behavior suggesting a multifractal character. We computed the fractal dimension at the different spatial resolutions obtaining a collapse at the different scales. Thus, the interfaces of constant Λ build a multifractal hierarchy and generalized scale invariance is present in the FSLE field. A second objective of this study was to quantify the impact of the uncertainties that can arise from numerous kind of errors in the velocity data on the FSLEs. This is done by introducing a random perturbation in the velocity data of the Eulerian model, and computing the relative error of the FSLE with this perturbation. We obtain that even for a perturbation of 10 times the velocity data the relative error of the FSLE is smaller than 25%, showing the robustness of the FSLE. At larger spatial resolution ($\delta_0 = 1/64°$) this relative error is about 45%. On the other side, missing spatial resolution of the velocity field generates a relative error with respect to the original field of 70% for a missing resolution of four times the original. The mesoscale structures remain even with this coarse spatial resolution. Unresolved small scales are included in the computation of the particle trajectories modelled as Lagrangian diffusion. The relative error of the FSLE with the eddy-diffusion corresponding to the resolution of the DieCAST model, is smaller than 45%. The main structures and locations of transport remain, although they became smeared out at smaller spatial resolution of the velocity data.

We have shown that due to its robustness and scale invariance, the FSLE is a powerful Lagrangian technique to study mixing and transport properties of the Sea surface.

Appendix A

Fourth-order Runge-Kutta method

The Runge-Kutta algorithm is a method to solve first-order differential equations (DE). The generic problem in ordinary differential equations is thus reduced to the study of a set of N coupled *first-order* differential equations for the functions $y_i, i = 1, 2, ..., N$, having the general form

$$\frac{dy_i(x)}{dx} = f_i(x, y_1, ...y_N), \qquad i = 1, ..., N \tag{A.1}$$

where the functions f_i are known.

Runge-Kutta methods propagate a solution over an interval by combining the information from several Euler style steps (each involving one evaluation of f_i), and then using the information obtained to match a Taylor series expansion up to some higher order. The formula for the Euler method is

$$y_{n+1} = y_n + hf(x_n, y_n), \tag{A.2}$$

which advances a solution from x_n to $x_{n+1} = x_n + h$. It advances the solution through an interval h, but uses derivative information only at the beginning of that interval.

The fourth-order Runge-Kutta method [38, 39] requires four evaluations of the functions f_i per step h:

$$\begin{aligned} k_1 &= hf(x_n, y_n) \\ k_2 &= hf(x_n + \frac{h}{2}, y_n + \frac{k_1}{2}) \\ k_3 &= hf(x_n + \frac{h}{2}, y_n + \frac{k_2}{2}) \\ k_4 &= hf(x_n + h, y_n + k_3) \\ y_{n+1} &= y_n + \frac{k_1}{6} + \frac{k_2}{6} + \frac{k_3}{6} + \frac{k_4}{6} + O(h^5)). \end{aligned}$$

Appendix B

Bilinear interpolation

We sometimes know the value of a function $f(x)$ at a set of points $x_1, x_2, ..., x_n$, but we don't have a analytic expression for $f(x)$ that let us calculate its value at an arbitrary point.

In multidimensional interpolation, we seek an estimate $y(x_1, x_2, ..., x_n)$ from an n-dimensional grid of tabulated values y and n one-dimensional vectors giving the tabulated values of each of the independent variables $x_1, x_2, ..., x_n$.

In two dimensions [39], we imagine that we are given a matrix of functional values $ya(j, k)$, where j varies from 1 to m, and k varies from 1 to n. We are also given an array $x1a$ of length m, and an array $x2a$ of length n. The relation of these input quantities to an underlying function $y(x_1, x_2)$ is

$$ya(j, k) = y(x1a(j), x2a(k)). \tag{B.1}$$

We want to estimate, by interpolation, the function y at some untabulated point (x_1, x_2).
An important concept is that of the grid square in which the point (x_1, x_2) falls, that is, the four tabulated points that surround the desired interior point. For convenience, we will number these points from 1 to 4, counterclockwise starting from the lower left. More precisely, if

$$x1a(j) \leq x_1 \leq x1a(j + 1)x2a(k) \leq x_2 \leq x2a(k + 1) \tag{B.2}$$

defines j and k, then

$$\begin{aligned} y_1 &\equiv ya(j, k) \\ y_2 &\equiv ya(j + 1, k) \\ y_3 &\equiv ya(j + 1, k + 1)) \\ y_4 &\equiv ya(j, k + 1). \end{aligned}$$

The simplest interpolation in two dimension is bilinear interpolation on the grid square. Its formulas are:

$$t \equiv (x_1 - x1a(j))/(x1a(j+1) - x1a(j)) u \equiv (x_2 - x2a(k))/x2a(k+1) - x2a(k)) \quad \text{(B.3)}$$

(so that t and u each lie between 0 and 1), and

$$y(x_1, x_2) = (1-t)(1-u)y_1 + t(1-u)y_2 + tuy_3 + (1-t)uy_4. \quad \text{(B.4)}$$

Appendix C

Heun's algorithm

The Heun's algorithm is a method to solve stochastic differential equations (SDE) based on the order two Runge-Kutta method for ordinary differential equations (ODE). A generic SDE has the following expression for a dynamical variable $x(t)$:

$$\frac{x(t)}{dt} = q(x,t) + g(x,t)\xi_w(t)$$

where $q(x,t)$ and $g(x,t)$ are functions, linear or non linear, and $\xi_w(t)$ is a white Gaussian noise, which properties are

$$\langle \xi_w(t)\xi_w(t')\rangle = 2D\delta(t-t')$$

A possible algorithm [30] to solve the SDE is

$$\begin{gathered} k = hq(t,x(t)) \\ l = h^{1/2}u(t)g(t,x(t)) \\ x(t+h) = x(t) + \tfrac{h}{2}\left[q(t,x(t)) + q(t+h,x(t)+l+k)\right] + \\ +\tfrac{1}{2}h^{1/2}u(t)\left[g(t,x(t)) + g(t+h,x(t)+l+k)\right] \end{gathered}$$

where h is the temporal step and $u(t)$ is a independent set of random Gaussian numbers with zero mean and variance equal to one.

Bibliography

[1] G. Falkovich, K Gawedzki, and M. Vergassola. Particles and fields in fluid turbulence. *Rev. Mod. Phys.*, 73:913 – 975, 2001.

[2] G. Buffoni, P. Falco, A. Griffa, and E. Zambianchi. Dispersion processes and residence times in a semi-enclosed basin with recirculating gyres: An application to the Tyrrhenian sea. *J. Geophys. Res.-Oceans*, 102:18699–18713, 1997.

[3] J.H. Lacasce. Statistics from Lagrangian observations. *Progress in oceanography*, 77:1–29, 2008.

[4] A. J. Mariano, A. Griffa, T. Ozgokmen, and E. Zambianchi. Lagrangian analysis and predictability of coastal and ocean dynamics 2000. *J. Geophys. Res*, 19:1114, 2002.

[5] C. W. Leong and J. M. Ottino. Experiments on mixing due to chaotic advection in a cavity. *J. Fluid. Mech.*, 209:463, 1989.

[6] S. Wiggins. *Chaotic Transport in Dynamical Systems*. Springer-Verlag, New York, 1992.

[7] G. Haller and A. Poje. Finite time transport in aperiodic flows. *Physica D*, 119:352–380, 1998.

[8] G. Haller. Finding finite-time invariant manifolds in two-dimensional velocity fields. *Chaos*, 10(1):99–108, 2000.

[9] G. Haller and G. Yuan. Lagrangian coherent structures and mixing in two-dimensional turbulence. *Physica D*, 147:352–370, 2000.

[10] G. Lapeyre. Characterization of finite-time Lyapunov exponents and vectors in two-dimensional turbulence. *Chaos*, 12(3):688–698, 2002.

[11] B. Joseph and B. Legras. Relation between kinematic boundaries, stirring, and barriers for the antartic polar vortex. *J. Atm. Sci.*, 59:1198–1212, 2002.

[12] T. Koh and B. Legras. Hyperbolic lines and the stratospheric polar vortex. *Chaos*, 12(2):382–394, 2002.

[13] E Aurell, G Boffetta, A Crisanti, G Paladin, and A Vulpiani. Predictability in the large: an extension of the Lyapunov exponent. *J. Phys. A*, 30:1–26, 1997.

[14] G. Boffetta, G. Lacorata, G. Redaelli, and A. Vulpiani. Detecting barriers to transport: a review of different techniques. *Physica D*, 159:58–70, 2001.

[15] V Artale, G Boffetta, A Celani, M Cencini, and A Vulpiani. Dispersion of passive tracers in closed basins: Beyond the diffusion coefficient. *Phys. Fluids*, 9:3162–3171, 1997.

[16] F. d'Ovidio, V. Fernández, E. Hernández-García, and C. López. Mixing structures in the

mediterranean sea from finite-size lyapunov exponents. *Geophys. Res. Lett.*, 31:L17203, 2004.

[17] A. García-Olivares, J. Isern-Fontanet, and E. García-Ladona. Dispersion of passive tracers and Finite-Scale Lyapunov Exponents in the Western Mediterranean sea. *Deep-Sea Res. II*, 54:253–268, 2005.

[18] F. d'Ovidio, J. Isern-Fontanet, C. López, E. Hernández-García, and E. García-Ladona. Comparison between Eulerian diagnostics and Finite-Size Lyapunov Exponents computed from altimetry in the Algerian basin. *Deep-Sea Res. I*, 56:15–31, 2009.

[19] F.J. Beron-Vera, M.J. Olascoaga, and G.J. Goni. Oceanic mesoscale eddies as revealed by lagrangian coherent structures. *Geophys. Res. Lett*, 35:L12603, 2008.

[20] A. C. Haza, A. C. Poje, T. M. Özgökmena, and P. Martin. Relative dispersion from a high-resolution coastal model of the Adriatic Sea. *Ocean Modell.*, 22:48–65, 2008.

[21] A.M. Lyapunov. *The general Problem of the Stability of Motion*. Taylor and Francis, Washintong, 1992.

[22] V.I. Oseledec. A multiplicative ergodic theorem: Lyapunov characteristic numbers for dynamical systems. *Trans. Moscow Math. Soc.*, 19:197–231, 1968.

[23] L. Barreira and Ya.B. Pesin. *Lyapunov Exponents and Smooth Ergodic Theory.* University Lecture Series, American Mathematical Society, Providence, R.I., 2002.

[24] D. Halpern. *Satellites, Oceanography and Society*. Elsevier Sci., New York, 2000.

[25] D. B. Haidvogel. *Numerical Ocean Circulation Modeling*. Imperial College Press, London, 1999.

[26] D.E. Dietrich. Application of a modified "a" grid ocean model having reduced numerical dispersion to the Gulf of Mexico circulation. *Dyn. Atmos. Oceans*, 27:201–217, 1997.

[27] A. M. Mancho, D. Small, and S. Wiggins. A tutorial on dynamical systems concepts applied to lagrangian transport in ocean flows defined as finite time data sets: theoretical and computacional issues. *Physics Report*, 437:55–124, 2006.

[28] U. Frisch. *Turbulence: The Legacy of A.N. Kolgomogorv.* Cambrige University Press, 1995.

[29] A. L. Barabasi and H. E. Stanley. *Fractal Concepts in Surface Growth*. Cambrige University Press, 1995.

[30] M. San Miguel and R. Toral. *Stochastic Effects in Physical Systems, Instabilities and nonequilibrium structures*. Kluwer Academic Publisher, pp. 35-130, 2000.

[31] A. Okubo. Oceanic diffusion diagrams. *Deep-Sea Res.*, 18:789, 1971.

[32] J. Schneider, V. Fernández, and E. Hernández-García. Leaking method approach to surface transport in the Mediterranean Sea from a numerical ocean model. *J. Mar. Syst.*, 57:111–126, 2005.

[33] A.M. Mancho, E. Hernández-García, D. Small, S. Wiggins, and V. Fernández. Lagrangian transport through an ocean front in the North-Western Mediterranean Sea. *J. Phys. Oceanogr.*, 38:1222–1237, 2008.

[34] P. Brasseur, J.M. Beckers, J. M. andBrankart, and R. Shoenauen. Seasonal temperatures

and salinity fields in the Mediterranean sea: climatologycal analysis of a historical data set. *Deep-Sea Res.*, 43:159–192, 1996.

[35] E. Ott. *Chaos in Dynamical Systems*. Cambridge Univ. Press, Cambridge (UK), 1993.

[36] H. Turiel, A. Yahia and C.J. Pérez-Vicente. Microcanonical multifractal formalism-a geometrical approach to multifractal systems: Parti. syngularity analisis. *J. Phys. A: Math. Theor.*, 41, 2007.

[37] A. Griffa. Applications of stochastic particle models to oceanographic problems. In R. Adler, P. Muller, and B. Rozovskii, editors, *Stochastic modelling in physical oceanography*. Birkhauser, 1996.

[38] Richard C. DiPrima William E. Boyce. *Ecuaciones diferenciales y problemas con valores en la frontera*. Noruega Editores, Mexico, 1998.

[39] William T. Vetterling Willians H. Press, Saul A. Teukolsky. *Numerical Recipes in Fortran90*. Oxford University Press, London, 1996.